The effect of inclination and stand-off on the dynamic response of beams impacted by slugs of a granular material

T. Uth[a*], H.N.G. Wadley[b] and V.S. Deshpande[a]

[a] *Department of Engineering, University of Cambridge, Trumpington Street, Cambridge CB2 1PZ, UK*

[b] *Department of Material Science & Engineering, School of Engineering and Applied Science, University of Virginia, Charlottesville, VA 22904, USA*

Abstract

The dynamic response of end-clamped sandwich and monolithic beams to impact by high-velocity tungsten carbide (WC) particle columns (slugs) has been measured with the aim of developing an understanding of the interaction of ejecta from a shallow-buried explosion with structures. The monolithic beams were made from stainless steel, while the sandwich beams of equal areal mass comprised stainless steel face sheets and an aluminium honeycomb core. High-speed imaging was used to measure the transient transverse deflection of the beams, to record the dynamic modes of deformation, and to observe the flow of the WC particles upon impact. The experiments show that sandwich beams deflect less than the monolithic beams both in normal and inclined impact situations. Moreover, the deflections of all beams in the inclined orientation were less than their respective deflections in the normal orientation at the same slug velocity. Intriguingly, the ratio of the deflection of the sandwich to monolithic beams remains approximately constant with increasing slug velocity for inclined impact but increases for normal impact; i.e. inclined sandwich beams retain their advantage over monolithic beams with increasing slug velocity. Dynamic force measurements reveal that (i) the momentum transferred from the impacting slug to both monolithic and sandwich beams is the same, and (ii) the interaction between the impacting particles and the dynamic deformation of the inclined monolithic and sandwich beams results in a momentum transfer into these beams that is equal to or greater than the momentum of the slug. These experimental findings demonstrate that contrary to intuition and widespread belief, the performance enhancement obtained from employing beam inclination is not due to a reduction in transferred momentum. Finally, we show that increasing the stand-off distance decreases beam deflections. This is because the slugs lengthen as they traverse towards their target and thus the duration of loading is extended with increasing stand-off. However, combining increased stand-off with sandwich construction does not yield the synergistic benefits of sandwich construction combined with beam inclination.

Keywords: particle impact; V-hull design; hydrodynamic loading; liquid-like; momentum transfer

* Corresponding author. Tel.: +44 1223 748241. E-mail address: thu21@cam.ac.uk.

1 Introduction

The design of vehicle underbody structures that can survive the impact of soil ejected by shallow-buried explosives has been a topic of considerable interest for many years. Several strategies have been recently investigated to improve the blast resistance of these underbody structures without increasing the overall weight of the vehicles. These include: (i) replacing the monolithic underbody by a sandwich panel (Dharmasena et al., 2013; Liu et al., 2013; Rimoli et al., 2011; Wadley et al., 2013), (ii) increasing the so-called stand-off of the vehicle floor from the ground (Børvik et al., 2011; Dharmasena et al., 2013; Hlady, 2004; Pickering et al., 2012), and (iii) inclining the underbody with respect to the ground by making use of a V-shaped hull design (Anderson et al., 2011; Bergeron and Tremblay, 2000; Follett, 2011; Fox et al., 2011) as sketched in Fig. 1. The purpose of this experimental study is to examine the relative efficacies of each of these concepts both independently and in combination using a novel laboratory-based approach.

The phenomena leading to dynamic loading of a structure following detonation of nearby shallow-buried explosives are very complex, but can be separated into three sequential phases: (i) transfer of impulse from the explosive to the surrounding soil, leading to the formation of a dispersion of high-velocity soil particles; (ii) propagation and expansion of the soil ejecta; and (iii) impact of the soil ejecta against the structure with attendant momentum transfer (Deshpande et al., 2009). Experimental (Bergeron and Tremblay, 2000; Reichenbach et al., 1991) and numerical (Børvik et al., 2011; Fairlie and Bergeron, 2002) studies have shown that soil impact is responsible for a substantial fraction of the blast load applied to a target structure. Moreover, empirical models that predict the impulsive loads imposed by soil ejecta (Westine et al., 1985) as well as to structural design codes such as the one proposed by Morris (1993) have helped inform more recent experimental characterizations of buried explosive events (Bergeron et al., 1998; Neuberger et al., 2007).

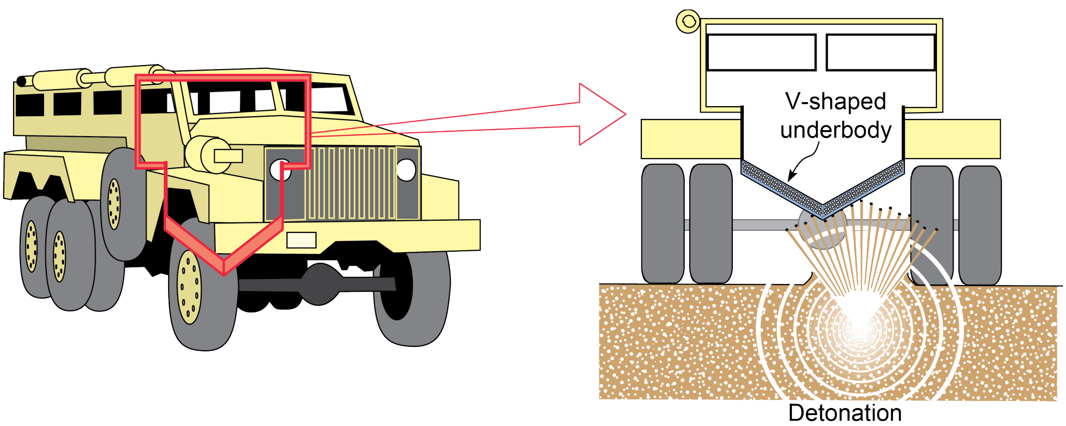

Fig. 1. Schematic illustration of a vehicle with V-shaped underbody designed to protect against the soil ejecta generated by the detonation of a shallow-buried explosive.

Following the work on water blast (Fleck and Deshpande, 2004; Wadley et al., 2008; Wei et al., 2008; Xue and Hutchinson, 2004) and air blast (Dharmasena et al., 2011, 2008; Kambouchev et al., 2007), a number of recent experimental and numerical studies (Dharmasena et al., 2013; Liu et al., 2013; Rimoli et al., 2011; Wadley et al., 2013) suggest that some sandwich structures outperform monolithic structures of equal mass when subjected to high-velocity soil loading representative of a landmine explosion. Numerical calculations (Dharmasena et al., 2013; Liu et al., 2013) have shown that this performance benefit is not related to a fluid-structure interaction effect as in the water blast problem, but arises from the higher bending stiffness and strength of sandwich structures compared to monolithic counterparts of equal mass per unit area. Experimental studies have also shown that increasing the stand-off distance between the target and the explosive/ground decreases the deflections of monolithic plates (Børvik et al., 2011; Fourney et al., 2005; Pickering et al., 2012) and sandwich panels (Dharmasena et al., 2013). Traditionally, this decrease has been attributed to a reduction in the momentum transfer from the ejected soil and detonation products to the target due to the spherical expansion of the ejecta; see experiments of Hlady (2004) for rigid targets and Pickering et al. (2012) for deformable plates. However, there is an additional factor that leads to reduced deflections with increasing stand-off. Measurements by Taylor et al. (2010) and McShane et al. (2013) have shown that velocity gradients within the soil ejecta tend to spread out the ejecta in the radial direction with increasing stand-off, thereby increasing the loading time and reducing the pressure imposed by the ejecta on the targets. Numerical calculations of Liu et al. (2013) and Dharmasena et al. (2013) have shown that for a given impulse, the plate deflections decrease with increasing loading time and thus Dharmasena et al. (2013) have argued that these radial velocity gradients are an additional factor leading to the observed reduction in plate deflections with increasing stand-off.

Armoured vehicles often employ V-shaped hull designs (Fig. 1) because there is considerable evidence that such constructions significantly enhance the survivability of vehicles subjected to blast from buried explosives. However, there is a paucity of data in the open literature, with most such studies restricted to rigid targets. These experiments (Genson et al., 2008; Anderson et al., 2011; Fox et al., 2011) suggest that the momentum transferred from the ejecta into an inclined rigid target is less than that transferred into a normally oriented target. Benedetti (2008) and Follet (2011) have reported measurements for the performance of V-hulls made from aluminium sheets and composite materials, respectively. However, to date, no systematic studies on the effect of inclination and the origins of the observed benefits of V-hull construction have been reported for deformable targets. Moreover, any potential benefits that might be accrued by the combination of sandwich construction with V-hull design remain scientifically unexplored.

The data in the literature suggests that the key factor contributing to the superior performance of V-shaped hulls is the reduction in the momentum transferred into such structures. Non-cohesive granular materials impinging on an inclined rigid plane generate flow patterns similar to those observed for fluid jet impacts (Cheng et al., 2007; Johnson and Gray, 2011). Implicitly using this analogy, Tremblay (1998) predicted a dramatic reduction of the momentum transferred to a rigid target with increasing obliquity. However, the dynamic deformation of non-rigid targets subjected to liquid-jet impact can result in significant enhancements of the momentum transfer, as shown recently by Uth and Deshpande (2013). Moreover, no measurements of the momentum transfer have been reported to confirm the fidelity of the analogy between the impact of a liquid jet and that of granular material. Measurements of momentum transfer into deformable inclined targets combined with dynamic visualization of the deformations from well-characterized granular column impacts will aid our fundamental understanding of the response of V-shaped hull structures to such loadings.

1.1 Scope of study

The study investigates the two key concepts currently employed to enhance the survivability of underbody vehicle structures to landmine explosions, viz. inclination of the structure with respect to the incoming granular spray and enhanced stand-off between underbody and ground. In addition, we also investigate whether the use of sandwich structures in combination with these two concepts would give further improvements in performance. We emphasize that the main aim of this paper is to present detailed measurements, which are not possible under field conditions, of the interaction of high velocity granular media with structures. Hence the loading conditions, structures etc. used in this laboratory investigation do not reflect field conditions, e.g. the experiments here use granular media comprising particles of density $16\ \mathrm{g\,cm^{-3}}$ impacting targets at velocities in the range $60\ \mathrm{ms^{-1}}$ – $100\ \mathrm{ms^{-1}}$ while in typical field conditions the soil particles of density approximately $3\ \mathrm{g\,cm^{-3}}$ impact structures at velocities of about $600\ \mathrm{m\,s^{-1}}$. However, the results are intended to give insight into the dynamic fluid-structure interaction processes as well as provide detailed measurements for validating future numerical models.

The outline of the paper is as follows. First we describe the design of the monolithic and sandwich beams used in this study as well as the experimental set-up used to load these beams via high-velocity granular slugs comprising tungsten carbide (WC) particles (these high-density slugs have a momentum comparable to the momentum imparted to structures in landmine loading events). The set-up includes a system of load cells that can measure the momentum components transferred from the slug into the beam for both normal and inclined impacts. Measurements of the response of the beams subjected to normal and inclined impact are then described and finally the effect of stand-off is quantified.

2 Experimental protocol

Cylindrical slugs comprising WC particles were impacted against rigid, monolithic and sandwich beams; their dynamic responses were measured in terms of deflection and transmitted momentum. We use high-density WC particles ($\sim 15\times 10^{3}\ \mathrm{kg\,m^{-3}}$) to increase the impact momentum range attainable in this study. Figure 2 depicts the experimental set-up, which comprises four main components (from right to left): (i) a gas gun to fire a solid projectile, which then accelerates the piston of (ii) a slug launcher apparatus based upon that developed by Park et al. (2013); (iii) a WC slug that initially rests inside the cylindrical cavity of the launcher; and (iv) the beams clamped to the support rig, which is equipped with force sensors to measure the transferred momentum. We now proceed to describe the manufacture of the beams and each of the four components listed above.

2.1 Beam manufacture

Sketches of the "rigid", sandwich and monolithic beam type investigated in this study are included in Fig. 3. All three beams had a free span of $2\ell = 100$ mm and a width (in the x-direction of Fig. 2) of 21.3 mm. In addition, the two deformable beams (sandwich and monolithic) had identical areal masses of $m = 5.6\ \mathrm{kg\,m^{-2}}$. The rigid beam was machined from a solid block of aluminium alloy and served as a reference to quantify the momentum transmitted into a nominally rigid structure. Sandwich beams comprised two identical AISI 304 stainless steel face sheets of thickness $H_f = 0.3$ mm and an aerospace grade aluminium honeycomb core (grade 3.1-1/8-07N-5052[1]), which had a thickness of $H_c = 10.3$ mm and density of $\rho_c = 50\ \mathrm{kg\,m^{-3}}$. The honeycomb core was oriented such that the so-called out-of-plane direction of the honeycomb was parallel to the thickness direction of the beam and the honeycomb walls of double thickness parallel to the longitudinal axis of the beam, as shown in the inset in Fig. 3b.

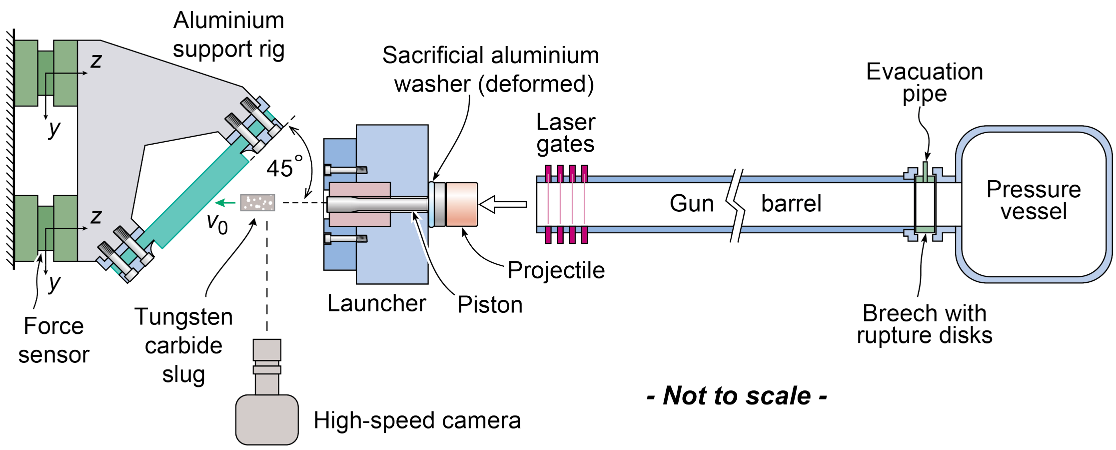

Fig. 2: Sketch of the overall set-up used to measure the response of clamped beams impacted by high-velocity slugs of tungsten carbide particles. The set-up includes a gas gun to fire the projectile, a launcher to generate the slug, and a support rig to clamp the beams. The impact event is imaged using a high-speed camera and the projectile velocity is measured using laser gates.

The manufacture of the sandwich beams was as follows. Face sheets were cut into rectangles of length 180 mm ± 1 mm (SD) and width 21.3 mm ± 0.1 mm using a sheet metal guillotine. The honeycomb cores were cut to size using the blade of a Stanley snap-off knife and had portions of size 40 mm × 15 mm removed from the ends of the 180 mm × 21.3 mm × 10.3 mm cuboids. The sandwich beams were manufactured by adhesively bonding two identical face sheets to the honeycomb cores using an adhesive film (Redux 312L[2]), which contributed an areal mass of $0.15\ \mathrm{kg\,m^{-2}}$ (the areal mass of the sandwich beams quoted above

[1] Amber Composites Ltd., 94 Station Rd, Langley Mill, Nottingham, NG16 4BP
[2] Hexcel Composites Ltd., Cambridge CB22 4QD, UK.

includes the mass of this adhesive). The sandwich assembly was oven-cured at 120°C for about 30 minutes. After curing, the 40 mm end portions of the beams were filled with an epoxy resin (Biresin G30[3]), as indicated in Fig. 3b, to allow clamping pressures higher than the compressive strength of the sandwich core to be applied.

The equal mass monolithic beams were made from the same material as the face sheets of the sandwich beam and had a thickness 0.7 mm. The manufacture of the monolithic beams simply involved the guillotining of the 0.7 mm AISI 304 stainless steel sheets into rectangles of length 180 mm ± 1 mm and width 21.3 mm ± 0.1 mm. The material properties of the constituents of the sandwich beams and the monolithic beams are detailed in the Appendix. We note in passing that the sandwich and monolithic beams tested in this study are significantly more compliant than the structures used in armoured vehicles. This was necessary considering the significantly lower impact velocities employed in this laboratory scale study, to approximately replicate the deformations that occur in vehicle structures subjected to landmine explosions.

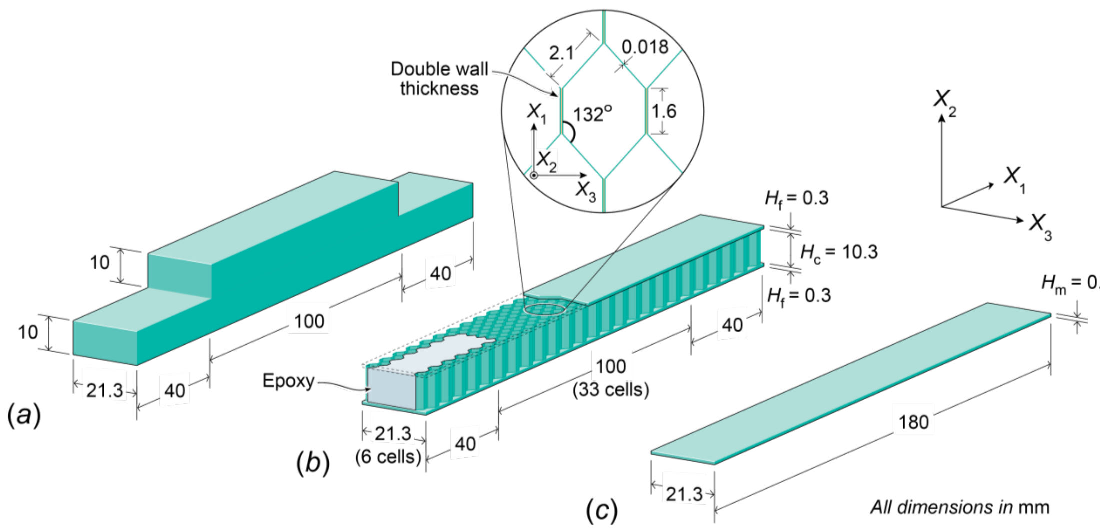

Fig. 3. Sketches of the (a) rigid, (b) honeycomb core sandwich and (c) monolithic beam types investigated here. In part b, the epoxy-filled end sections of the beam along with an inset to show the details of the honeycomb core are sketched; the global coordinate system (X_1, X_2, X_3) is indicated on the right.

2.2 Dynamic experimental set-up

We proceed to briefly describe the four main components of the experimental set-up sketched in Fig. 2.

<u>Slug launcher</u>: The launcher was modified from that developed by Park et al. (2013) and later employed by Uth and Deshpande (2014); here we briefly describe it with an emphasis on the modifications made as part of this study. A cross-sectional view of the slug launcher is

[3] Sika Deutschland GmbH, Stuttgarter Str. 139, Bad Urach, 72574, Germany.

sketched in Fig. 4. It comprised a cylindrical cavity for the WC slug and a piston to push the slug out of the cavity when a projectile, fired from a gas gun, impacted the piston head. The launcher was bolted to a rigid support frame so that it remained stationary during the impact event. Unless otherwise stated, all components were made from low-carbon steel. The launcher consisted of a thick-walled circular cylinder with an exchangeable barrel of inner diameter 12.7 mm and length 50 mm. The piston had three distinct segments: a front, middle and back. The front segment was 20 mm long and of diameter 12.7 mm (H7/h6 fit with cylinder cavity); it slides smoothly within the exchangeable inner barrel of the launcher. An anti-seizing compound was applied to the front end of the piston to reduce friction with the cylinder walls and to avoid galling. The middle segment, with a length of about 50 mm had been turned down to a diameter of 10.5 mm so that there was a 1.1 mm clearance with the cavity wall. This reduction in the diameter was needed to prevent jamming of the piston inside the cylindrical cavity after impact of the projectile: the high-speed impact of the projectile results in fattening of the piston rod near the impacted end. The piston head at the back acts as an end-stop to arrest the piston. In addition, a 5 mm thick Al alloy washer of inner diameter 12.7 mm and outer diameter 25 mm (equal to that of the piston head) was slid onto the piston until it was snug against the piston head. This washer cushioned the impact of the piston head against the launcher. A retainer was bolted to the front of the main part of the launcher to hold the exchangeable barrel in place. Before the launch process, the slug sat inside the exchangeable barrel such that there was a 10 mm gap between the front of the slug and the end of the exchangeable barrel: trial-and-error experimentation showed that this extra cavity length helped to maintain the shape of the launched slug. Furthermore, the WC particles abrade the inner wall of the exchangeable inner barrel and hence it was replaced after every three tests to ensure a good sliding fit between the piston and the barrel.

Tungsten carbide (WC) slugs: The slugs of mass $m_{slug} = 22.72$ g comprised mainly WC particles with a size range of 45-150 μm as well as trace quantities of silica sand and icing sugar (see Table 1 for the exact composition). The silica particles were added as tracer particles to aid the visualisation of the slug deformation, while the sugar helped to maintain the slug shape before it was launched. The slugs were prepared as follows. First, scratches on the inner surface of the exchangeable barrel originating from previous tests were removed with a hand reamer (Ø 12.7 mm) and then the front of the cavity was closed with a plug of length 10 mm (not shown). Next, 0.02 g of sugar were spread evenly over the surface of the plug inside the barrel. The WC particles were then compacted in 5 layers by repeatedly dropping a 12.6 mm diameter steel rod from a few millimetres height. After each layer of WC was compacted, one quarter of the total mass of silica sand tracer particles were placed along the periphery of the WC layer. This ensures that most tracer particles appear on the outside of the slug during flight. The piston (Fig. 4) was pushed firmly against the free surface of the WC slug and while holding the piston in place, the launcher was flipped over and the plug was removed. Finally, the icing sugar that covers the free surface of the WC slug, was moistened utilising a water spray bottle. The moistened layer was then dried by putting the launcher for 1 hour into an oven at 100°C. The bonds created between the WC particles by the dried sugar were found to provide enough strength to maintain the shape of the slug during test set-up. However, these weak and brittle bonds break during the launch process and, consequently, have insignificant effects thereafter. The slug height achieved by this procedure was 20.0 mm ± 0.1 mm and the resulting density of the slug was 8900 kg m^{-3} ± 96 kg m^{-3}, corresponding to a solid fraction of 57.4 % ± 0.6 %. The compressive response of the slugs subjected to uniaxial straining is given in the Appendix.

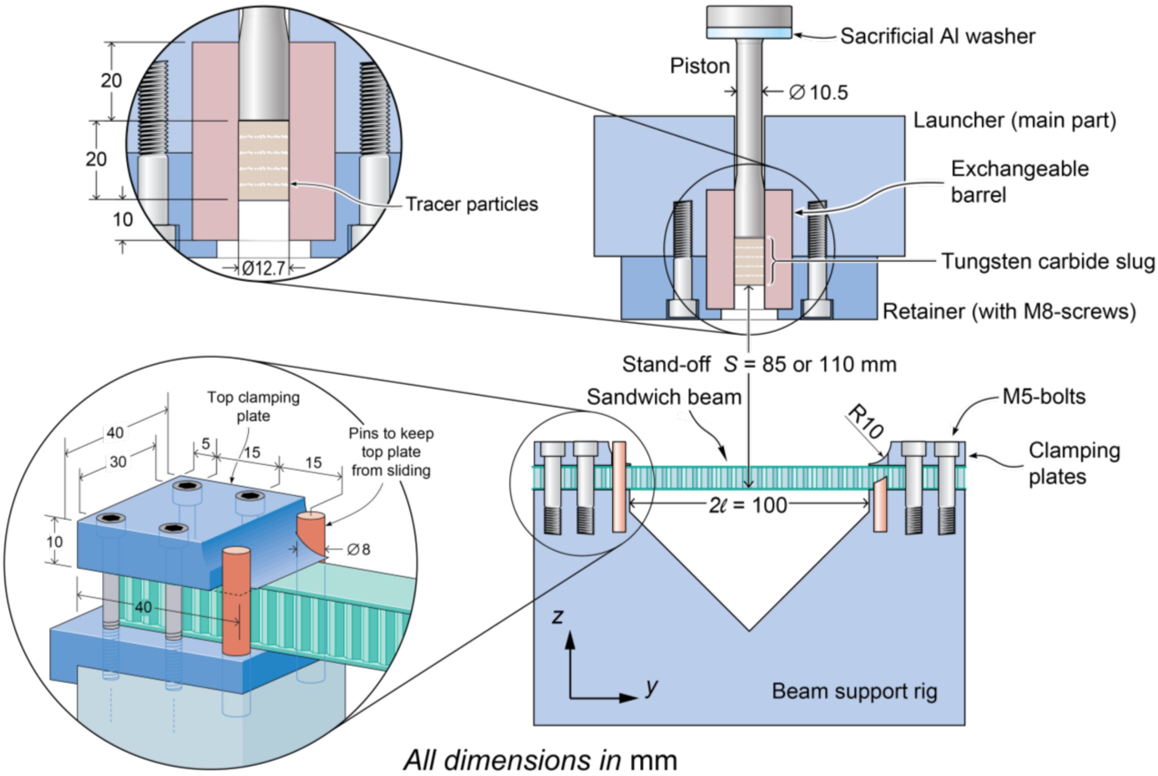

Fig. 4. A sketch showing a cross-sectional view of the slug launcher and a clamped sandwich beam impacted in the normal orientation. Detail views of the clamping set-up and the inner barrel with the slug at rest are included.

Table 1. Constituents of the slug.

Constituent	Abbreviation	Particle density (kg m^{-3})	Particle size (μm)	Mass per slug (g)
Tungsten carbide	WC	15630	45-150	22.6
Silica sand	sand	2650	150-300	0.1
Icing sugar	sugar	1600	10-30	0.02

Gas gun to fire projectile: The steel projectile of mass 105 g and diameter 28.4 mm was accelerated using a gas gun with a barrel length of 4.5 m and inner diameter of 28.5 mm, as shown in Fig. 2. No sabot was employed and the breach mechanism of the gun was formed by bursting copper diaphragms. The impact velocities v_p of the projectile against the piston of the launcher ranged from 150 m s^{-1} to 230 m s^{-1}; the velocity of the projectile was measured at the exit of the barrel using laser gates. The impacted end of the piston was placed about 25 mm in front of the end of the gun barrel. The flight of the WC slug and the profile views of the transient deflection of the beams were visualized using a Phantom v1610 digital camera[4] with inter-frame times of 40 μs and exposure times of 1 μs.

Clamped beam support rig: Experiments were conducted with beams in one of two orientations (Fig. 5): some of the beams were oriented such that the slugs impacted at an angle $\alpha = 90^{o}$ to the longitudinal axis of the beam (referred to as the "normal" orientation) and others such that the slugs impacted at an angle $\alpha = 45^{o}$ (referred to as the "inclined" orientation[5]). The set-up comprises either a steel support rig of mass 5.3 kg for the normal impact case (Fig. 5a) or an aluminium rig of mass 2.3 kg for the inclined case (Fig. 5b). The support rigs are in turn supported on two 3-component piezoelectric force sensors (Kistler[6], type 9347C) that were used to measure the momentum transferred by the impacting slug into the beam and then into the support structure. These sensors measure forces in the three orthogonal directions (x, y, z), where the z-axis was always in the direction of the incoming slug and the y-axis was perpendicular to the z-axis in the plane of the beam, as shown in Fig. 5. The force sensors had capacities of 30 kN in the z-direction and 10 kN in the x- and y-directions. The output from the sensors was conditioned using a Kistler 5001 charge amplifier and recorded with a digital oscilloscope (Tektronix[7], TDS 3014B). The force transducers can only sustain a small bending moment. Thus, rather than clamping the beams directly onto the transducers, the force transducers were placed below the essentially rigid support rigs, so that minimal bending moments were transmitted into these transducers.

[4] Vision Research, Priory Business Park, Stannard Way, Bedford, MK44 3RZ, UK.

[5] 45^{o} is a high inclination angle for a vehicle underbody structure but such high angles are employed in certain vehicles such as the Casspir and the Buffalo (both are Mine Resistant Ambush Protected vehicles).

[6] Kistler Instruments Ltd., Hook, Hampshire RG27 9GR, UK

[7] Tektronix, P.O. Box 500, Beaverton, OR 97077, USA.

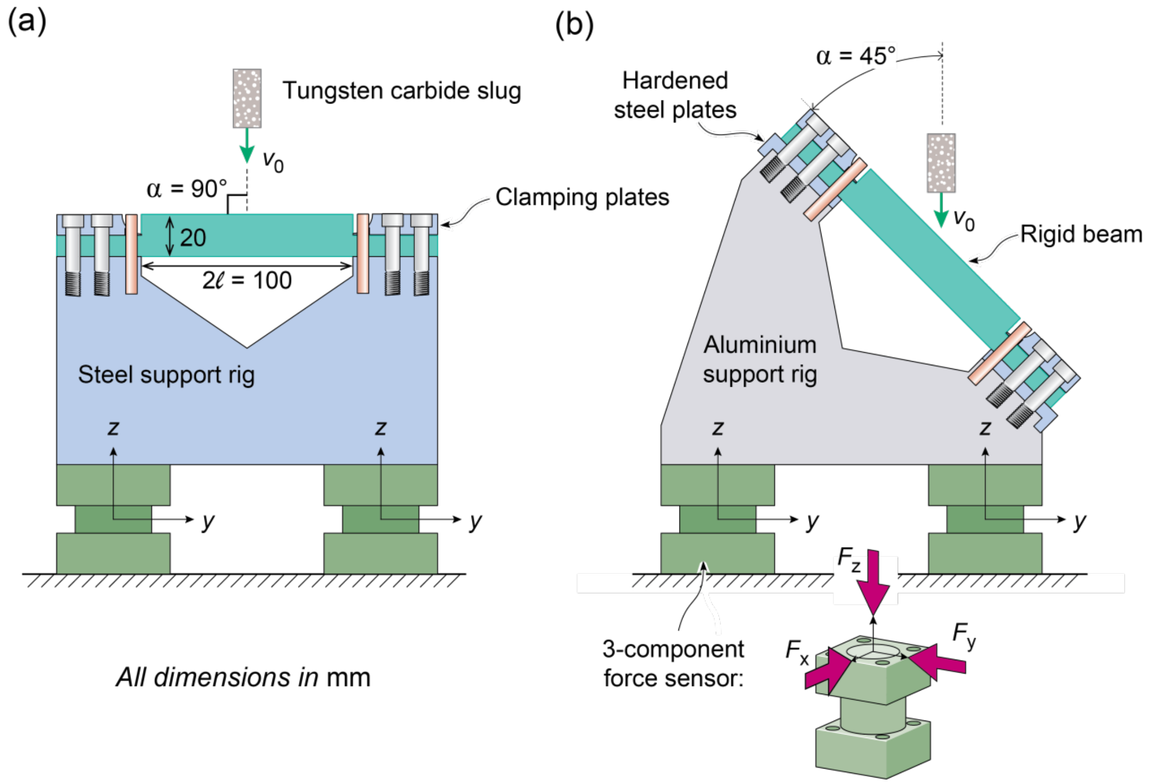

Fig. 5. Sketches of the clamped "rigid beams" in the (a) normal and (b) inclined orientations. The coordinate system fixed to the support structure (x, y, z) is sketched along with the piezoelectric force sensors used to measure the momentum transferred from the test beams into the support structure. The inset in part (b) shows a detailed view of the force sensors and the three components (F_x, F_y, F_z) of the measured forces.

2.3 Design of the beam clamps

Pull-out of a beam at its clamps can give rise to substantial out-of-plane deflections. To avoid this source of uncertainty in the experiments, particular care was taken to minimize pull-out at the clamps. The beam clamps were designed so as to minimize pull-out of the beams − the pull-out measured during quasi-static loading with a 12.7 mm diameter spherical indenter to an applied displacement of 15 mm was less than 2 μm for both beam designs. However, as discussed in Uth & Deshpande (2014) and Wadley et al. (2013), the clamping plates also needed to be designed to minimize interference with the WC particles when they flowed outwards from the impact site towards the supports. An interference with this flow causes particle redirection and increased momentum transfer, which may result in premature failure near the supports (Wadley et al., 2013).

Different types of clamps were employed depending on the beam type and orientation. We briefly describe the designs used in this study:

(i) *Rigid beams*: To provide a baseline for the measurements of the transmitted momentum (i.e. so that the fluid-structure interaction effect due to the deformation of the beams can be quantified), a few tests were conducted with WC slugs impacting against nominally rigid beams in both the normal and inclined orientation. These nominally rigid beams (for the sake of brevity we subsequently shall refer to them as "rigid beams") were machined from a solid block of Al alloy to the dimensions shown in Fig. 3a. The width of the rigid beam was identical to that of the sandwich and monolithic beams (B = 21.3 mm). Details and dimensions of the clamping plates are shown in the inset in Fig. 4 (identical plates were used for normal impact against sandwich and monolithic beams). These plates were bolted to the support rig using four M5 bolts (grade 12.9) and a uniform clamping pressure of approximately 60 MPa was applied by tightening the bolts to 10.5 Nm using a torque wrench. In addition, the sliding of the clamping plates was reduced by using locating pins as shown also in the inset of Fig. 4. Note that the top surface of the rigid beams was level with the top of the clamping plate so that the outwards flowing WC particles were not impeded by the clamps (Fig. 5).

(ii) *Normal impact on sandwich and monolithic beams*: The deformable beams were clamped using the same clamping plates as the rigid beams. As seen from Fig. 4, the top surfaces of the deformable beams are not level with the top surface of the clamping plates; the fillet radius $R = 10$ mm put on the clamping plates prevents the outward flowing WC particles from coming to an abrupt stop.

(iii) *Inclined impact on sandwich and monolithic beams*: In this case, the majority of the WC particles flow in the downward z-direction (i.e. with a velocity in the same sense as the incoming slug) and thus special care needs to be taken to ensure that the motion of these particles is not impeded subsequent to impact. Therefore, the clamping set-up in this case was asymmetrical: while the clamps described in the two preceding paragraphs were used for the end of the beam nearer the launcher, a different clamp design was used for the distal end of the beam. Sketches of these distal end clamps for the monolithic and sandwich beams are included in the insets in Figs. 6a and 6b, respectively. The monolithic beams were directly welded to sacrificial clamping plates, thus eliminating any obstruction to the flow of the WC particles. Similarly, for the sandwich beams, a clamp with an incline of 10° was employed (a perfectly flat clamping plate with a thin membrane between the two sections through which the bolts pass would not be capable of applying the required clamping pressures). Initial tests confirmed that due to the deformation of the sandwich beams, the WC particles flow downwards at an angle greater than 15° with the front face of the undeformed sandwich beam. Consequently, this clamping plate does not interfere with the flow of the WC particles.

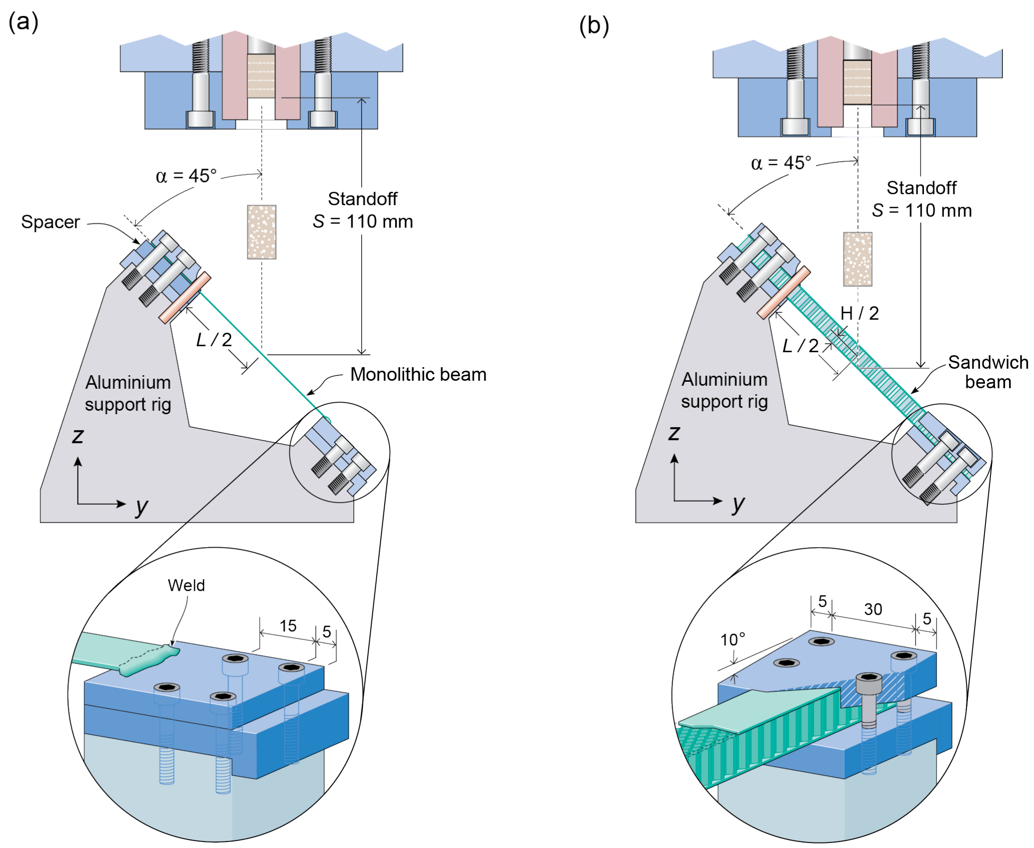

Fig. 6. Sketches of the loading set-up and support structure for impact tests on the inclined (a) monolithic and (b) sandwich beams. The sketches include partial section views of the slug launcher with the stationary WC slug and the definition of the stand-off distance S. Both parts of the figure include insets with a detail view of the clamps at the distal end.

The stand-off S of the beams in the normal and inclined orientation is defined in Figs. 4 and 6, respectively; i.e. S is defined as the distance between the front of the stationary WC slug in the launcher to the *rear face* of the beam. For the normal impact case, the beams are positioned such that the centre line of the slug passes through the mid-span of the beam, while in the inclined case the centre line of the slug intersects the beams at mid-span at a distance $H/2$ from the rear face, where $H \equiv H_c + 2H_f$ (Fig. 6b). Tests with $S = 65$ mm and 110 mm are reported for the normal impact case, while for the inclined case only a stand-off of $S = 110$ mm was investigated.

2.4 Temporal evolution of the WC slugs

WC slugs were generated by firing projectiles with a velocity in the range 150 m s^{-1} - 230 m s^{-1} against the launcher piston. In line with observations made for silica sand slugs by Park et al. (2013) and Uth and Deshpande (2014), the velocity of the particles within the slugs remains temporally invariant after the slugs fully exit the launcher (i.e. the velocity of the slug is constant over the period during which observations can be made). Moreover, consistent with previous studies, the particles within the slug have nearly no radial velocity but their axial velocity is spatially varying. In order to quantify this spatial gradient of the axial velocities we use images from the high-speed camera to measure the velocities of tracer particles as follows. Consider a WC slug that has exited the launcher and has a current length L, as shown in the inset in Fig. 7a. The slug is divided into five segments of equal length and the axial velocities v_t of tracer particles at the boundaries between these segments is plotted as a function of the non-dimensional coordinate X/L, where X is the axial distance measured from the rear end of the slug. In the inset of Fig. 7a, a slug generated by a projectile with a velocity of $v_p = 170$ m s^{-1} is shown and the tracer particles used to measure v_t are indicated by circles. Measurements of v_t as a function of X/L are plotted in Fig. 7a for three selected values of v_p, which indicate that the axial velocity within the slug varied linearly with X such that the front end is moving faster than the rear end, i.e. the length L of the slug was increasing as it travelled from the launcher towards the target (i.e. a stretching slug). It is worth emphasizing here that since the velocities v_t are temporally invariant, the plots of v_t versus X/L are also temporally invariant.

While characterising the response of the beams impacted by these WC slugs, it is instructive to label the slugs in terms of the velocity of the slug rather than the velocity of the projectile v_p that generated the slug. Thus, we define a mean slug velocity v_o as the average of the velocities of the six tracer particles shown in Fig. 7a. This mean slug velocity v_o is plotted in Fig. 7b as a function of v_p for all the WC slugs generated as part of this investigation; it is apparent that mean slug velocities v_o in the range 60 m s^{-1} – 100 m s^{-1} were attained for the projectile velocities employed here.

Numerous studies (Liu et al., 2013; Qiu et al., 2005) have suggested that the dynamic response of beams is dependent on the free-field areal momentum I_o of the impacting medium. While the mean velocity v_o is indicative of I_o, the mass or density distribution along the slug is required to quantify the relation between I_o and v_o. Since we cannot refer the tracer particles back to their positions in the undeformed slug, we cannot determine the density distribution within the slugs from the measurements reported here. In order to determine I_o we adopt a strategy motivated by measurements reported for slugs of silica sand by Park et al. (2013). They impacted the silica sand slugs against a direct-impact Kolsky bar and measured the momentum transmitted into the bar by the slug, in addition to making a direct measurement of the free-field momentum from the velocity and density distribution within the slug. These measurements demonstrate that the transmitted momentum is equal to the free-field momentum (to within the accuracy of the measurements). Thus, we again use direct-impact Kolsky bar measurements to infer the free-field momentum I_o of the WC slugs.

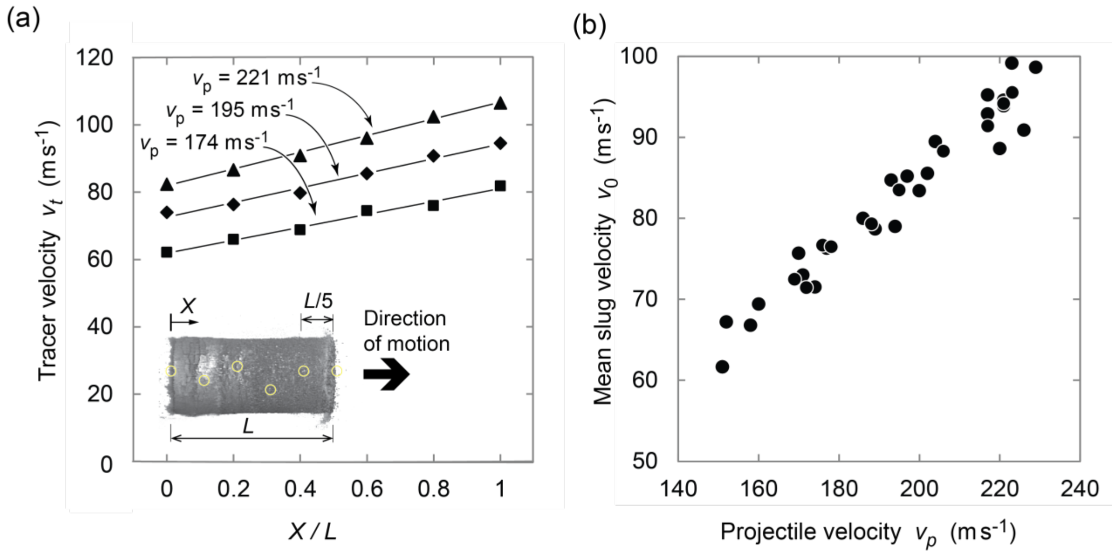

Fig. 7. (a) The measured axial velocities of the tracer particles in the WC slugs as a function of their non-dimensional position X/L. Measurements are shown for slugs generated by three projectile impact velocities v_p. The inset shows a slug of length $L = 27$ mm generated by a projectile velocity $v_p = 170$ m s^{-1} and the tracer particles are highlighted by circles. (b) The mean slug velocity v_o as a function of the projectile velocity v_p for all tests reported in this study.

The 12.7 mm diameter WC slugs were impacted normally and centrally against a stationary Al Kolsky bar of diameter 22.2 mm and length 2.2 m, which was placed at a distance S from the front end of the stationary slug inside the launcher as sketched in Fig. 8a. The transient axial force F generated within the Kolsky bar was measured via two semiconductor strain gauges[8], which were glued onto the bar 100 mm away from the impacted end and subsequently wired in a half-bridge configuration. Tensile wave reflections from the distal end of the bar, which complicate the interpretation of the measurements, reached the strain gauges after 680 μs. However, the loading pulses exerted by the WC slugs were always less than 600 μs and hence the full loading history of the slugs could be recorded using this set-up. We define the pressure p exerted by the slug as $p \equiv 4F/(\pi D^2)$, where $D = 12.7$ mm is the diameter of the slug. The measured temporal history $p(t)$ is plotted in Fig. 8b for two selected values of the mean slug velocity v_o and a stand-off of $S = 65$ mm. Time $t = 0$ corresponds to the instant that the slug impacts the Kolsky bar and the oscillations in the pressure history late in the impact event are due to spatial in-homogeneities in the sand slug density. For the higher value of v_o, the peak pressure exerted by the slug is higher, while the period over which the loading occurs is shorter. These two observations are rationalised as follows: (i) the loading due to the granular slug is primarily inertial (Park et al., 2013) and thus the impact pressure scales with the square of the particle velocity, i.e. impact pressure increases with v_o, and (ii) the loading time scales as L/v_o (Liu et al., 2013; Park et al., 2013; Uth and Deshpande, 2014) and is consequently longer for the lower impact velocity.

The transmitted areal momentum (taken here equal to the free-field areal momentum for the reasons detailed above) is given by

---

[8] AFP-500-090, Kulite Sensors Limited, Stroudley Rd., Basingstoke, Hants, RG24 8UG, UK

$$I_o = \int_0^\infty p(t)\, dt. \tag{2.1}$$

Measurements of I_o as function of the mean slug velocity v_o are included in Fig. 9a for two values of the stand-off S; these measurements indicate that there is a linear correlation between I_o and v_o. Recall that since we do not know the density distribution within the slug it is unclear whether v_o is a direct measure of the slug momentum. Thus, in order to further investigate this linear correlation we plot the ratio $\pi D^2 I_o/(4m_{slug})$ as function of v_o in Fig. 9b. Clearly, $\pi D^2 I_o/(4m_{slug}) \approx v_o$ over the entire range of slug velocities and the two stand-off distances considered here. Consequently, v_0 is a direct measure of the momentum of the WC slug that loads the beams, and thus in the remainder of this study we shall use v_o to label the slugs.

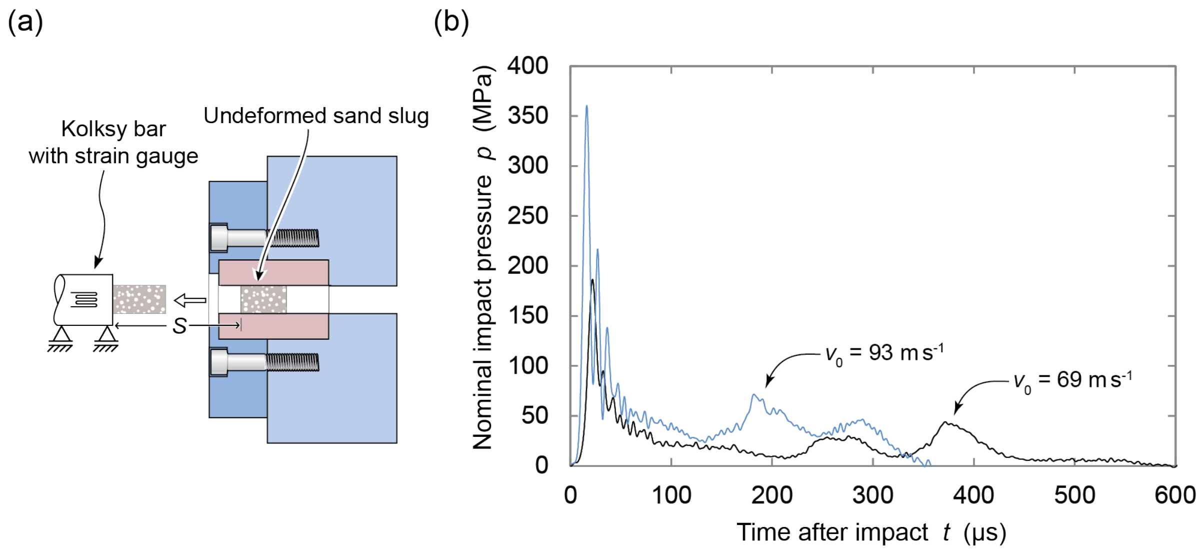

Fig. 8. (a) Sketch of the direct-impact Kolsky bar set-up used to measure the impact pressure versus time histories generated by the impact of the WC slugs. (b) The nominal pressure p versus time t histories exerted by WC slugs impacting the Kolsky bar at a stand-off $S = 65$ mm. Results are shown for slugs with two selected mean velocities v_o.

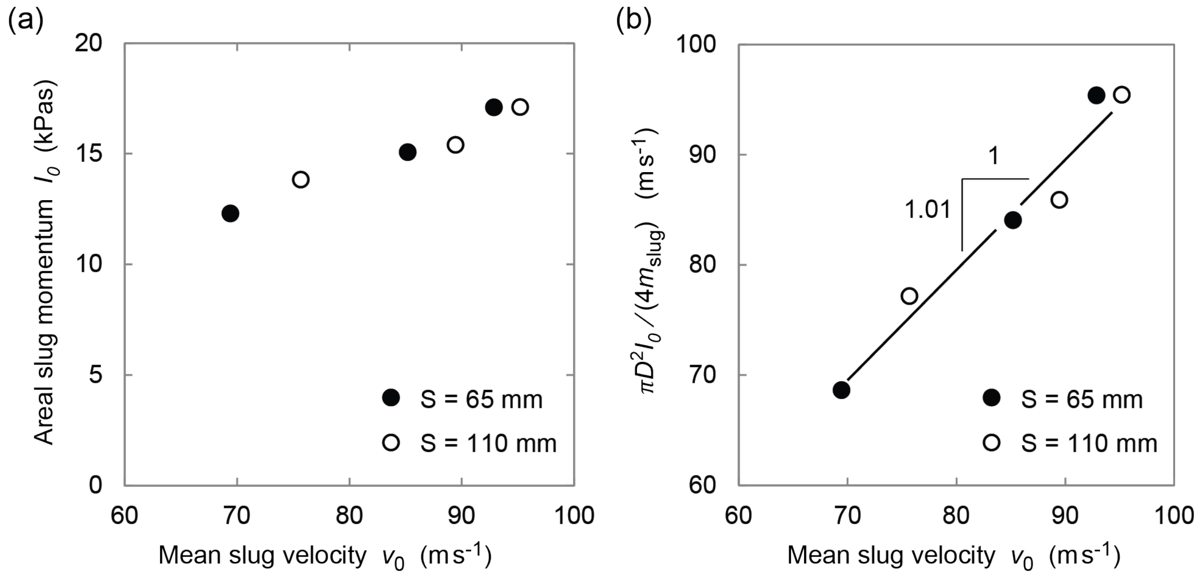

Fig. 9. (a) The measured areal slug momentum I_o as a function of the mean slug velocity v_o for the two values of stand-off S considered here. (b) A re-plot of the data shown in part (a) in terms of $\pi D^2 I_o/(4m_{slug})$ versus v_o to illustrate that $\pi D^2 I_o/(4m_{slug}) \approx v_o$ for the WC slugs considered in this study.

3 Effect of inclination on the response of the beams

We proceed to report observations and measurements of the response of the monolithic and sandwich beams in the normal and inclined orientations impacted by the WC slugs at a stand-off $S = 110$ mm. The mean slug velocities ranged from 67 m s^{-1} to 99 m s^{-1} corresponding to I_o ranging from 12 kPas to 18 kPas.

3.1 Measurements of the beam deflections

High-speed images of the impact of the $v_o \approx 70$ m s^{-1} WC slugs against the rigid, monolithic and sandwich beams in the normal orientation are included in Figs. 10a, 10b and 10c, respectively. The montages in Fig. 10 show images at four instants during the impact event, with time $t = 0$ corresponding to the instant the WC slug first impacts the beam. First, consider the case of the rigid beam shown in Fig. 10a. The beam undergoes no deformation; the slug spreads over the impacted surface of the beam and flows over the sides at times $t > 460$ μs[9]. Negligible rebound of the WC particles is observed. Next, consider the monolithic beam shown in Fig. 10b. Flexural hinges are seen to initiate near the impact site and travel towards the clamped supports. By $t = 760$ μs, these hinges had reached the supports and the beam continued to deflect in a string-like (membrane stretching) mode. Simultaneously, the WC slug continues to push against the beam and spreads along the

[9]The pile of particles seen in the images for $t \geq 460$ μs is not located on top of the beam, instead the particles pile up against a white background that is located 50 mm behind the beam – this background was added to improve the quality of the high-speed images.

deflected profile of the beam: this deformed profile being approximately V-shaped implies that the particles flow backwards (*flow reversal*) as the deflection of the beam increases. Again, the WC particles are seen to spill over the sides of the beam, which obscures the deflection measurement at mid-span of the beam. Some rebound of the granular medium was observed as the beam underwent a large deflection late in the interaction process ($t = 1760$ μs). The deformation of the sandwich beam, as shown in Fig. 10c, is similar to that of the monolithic beam with one key difference. Core compression is seen to occur which implies that the impacted face of the sandwich beam undergoes larger deflections compared to the back face. A comparison of the sandwich and the monolithic beam at $t = 1760$ μs indicates that larger flow reversal is caused by the large deflections of the front face of the sandwich beam.

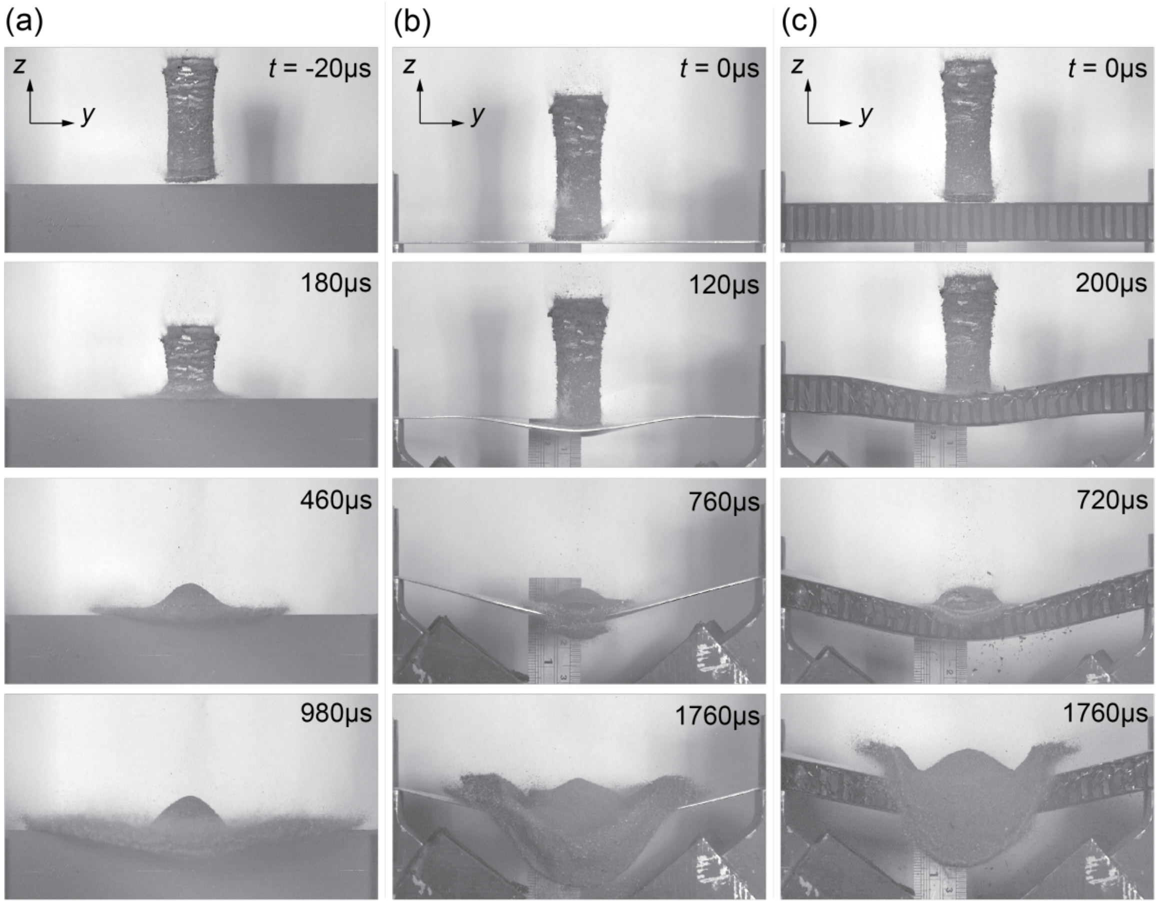

Fig. 10. High-speed images showing the normal impact of the $v_o \approx 70$ m s^{-1} slugs against the (a) rigid, (b) monolithic and (c) sandwich beam. Each image includes a time stamp, where time $t = 0$ corresponds to the instant that the slug first impacts the beam. The global coordinate system (x, y, z) from Fig. 5 is indicated in the first image of each part.

The temporal evolution of the deflection w at mid-span of the back faces of the monolithic and sandwich beam from Fig. 10 are plotted in Fig. 11. A comparison between the w versus t curves plotted for the monolithic and sandwich beam reveals two key differences: (i) the initial deflection rate of the sandwich beam is very small compared to the monolithic beam and (ii) even after the deflection rate of the sandwich beam increases, the maximum deflection attained by the sandwich beam is about a factor of 0.3 smaller than that of the monolithic beam. These observations can be rationalised via the high-speed images shown in Fig. 10. Upon initial impact of the WC slug, the honeycomb core of the sandwich beam immediately underneath the impact site compresses and the back face is loaded only through the sandwich core. This results in the so-called "soft-core" effect (Liang et al., 2007; Tilbrook et al., 2006): the back face is only slowly accelerated by the core because the core partially accommodates the deflection of the front face by compressing. When the back and front face velocities eventually equalize, the rate of deflection $\dot{w}$ increases. As elucidated in the numerical simulations of Liu et al. (2013), the smaller deflection of the sandwich beam compared to its monolithic counterpart is a result of the fact that for the level of loading applied here, the maximum deflection of the sandwich beam is on the order of the beam thickness (w ranges between $0.8H_c$ to $1.4H_c$). Thus, the deformation of the sandwich beam remains dominated by bending with the sandwich beam having a significantly higher bending strength and stiffness compared to its monolithic counterpart of equal areal mass.

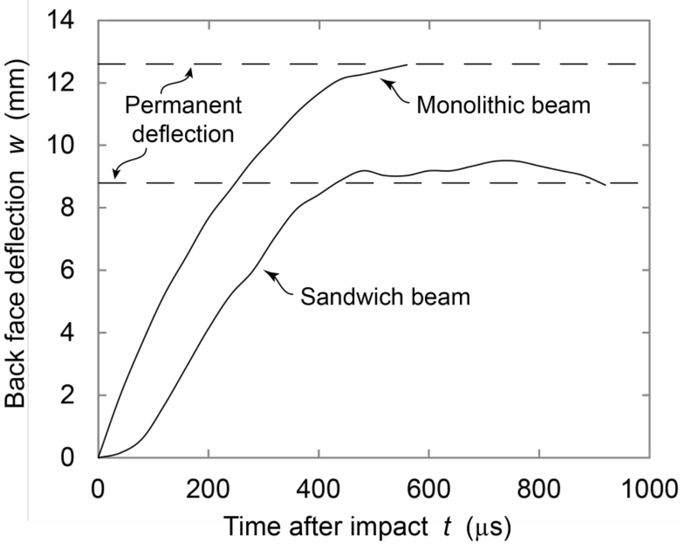

Fig. 11. The measured deflection w of the back faces at mid-span as a function of time t for the monolithic and sandwich beam shown in Fig. 10. The permanent deflections, measured after the beams were removed from the support rig, are marked by the dashed lines.

Next consider the montage of high-speed images for the impact of the $v_o \approx 100$ ms^{-1} slug[10] against the inclined rigid, monolithic and sandwich beams in Figs. 12a, 12b and 12c, respectively. Again, time $t = 0$ corresponds to the instant that the slug first impacts the beams. Of course, in this case one edge of the slug makes contact first and the deformation of the slug is localised at that edge as seen at $t = 20\ \mu$s in Fig. 12b. Subsequently, the slug spreads over the beam and the observations are similar to the normal impact case with the

[10] The images in Figs. 10 and 12 show the two extreme values of v_o and demonstrate that the shapes of the WC slugs prior to impact are qualitatively similar over the entire range of velocities investigated here.

following key differences: (i) the spreading of the slug is asymmetrical with the majority of the WC particles continuing to flow in the incidence (downward or negative z) direction, (ii) the deformation of both the monolithic and sandwich beam is asymmetrical with the maximum deflection not occurring at mid-span, and (iii) the location of the point of maximum deflection evolves with time, i.e. initially the point of maximum deflection occurs near the mid-span, but it then translates in the positive y- and negative z-direction (along with the flow of the majority of the WC particles) as time elapses. Thus, plotting the deflection of the location of a particular point on the beam, as done for the case of normal impact in Fig. 11, is no longer meaningful.

Photographs of the deformed monolithic and sandwich beams (after removal from the support rig) are included in Fig. 13 for both the normal and inclined impact cases. The photographs only show the span of the beam ($2\ell = 100$ mm) with the undeformed end portions of the beam that are within the supports excluded. The coordinate system corresponding to Fig. 3 is indicated in Fig. 13. In each case, photographs for two impact velocities v_o are included in parts (a) and (b) of Fig. 13 corresponding to the normal impact of the monolithic and sandwich beams, respectively. Analogously, in Figs. 13c and 13d, the corresponding images for the inclined impact are shown. While the photographs in Fig. 13 show the overall deformation including the deformation of the sandwich core, these side views fail to convey the three-dimensional nature of the deformation of these beams. Thus, in Fig. 14 we include section cuts of these same beams from X-ray computed tomography scans. These X-ray images show the sections of the beams in the $X_1 - X_2$ plane (at mid-width) and the $X_2 - X_3$ plane (while in most cases these sections are shown at mid-span, additional sections at selected locations are shown for the sandwich beams impacted at $v_o \approx 95$ m s^{-1} and 99 m s^{-1})[11]. We now proceed to discuss the deformation modes with reference to these images.

First consider the normal impact case. The monolithic beam deforms mainly in the $X_1 - X_2$ plane with the maximum deflection occurring in the symmetry plane at mid-span. In addition, some "dishing"-type deformation occurs as seen by the curvatures of the deformed beams in the $X_2 - X_3$ plane (Fig. 14a). The sandwich beams are seen to deflect by a combination of bending, core shear (which occurs mainly near the supports), and core compression (which is maximum at mid-span). The X-ray images in Fig. 14b show that, while the front face of the sandwich beam undergoes dishing (towards the centre of the beam), the back face undergoes negligible dishing in the $X_2 - X_3$ plane. This indicates that core compression, especially at mid-span, is non-uniform across the width of the beam and is a maximum at the geometrical centre of the beam.

[11] Using X-ray tomography, the honeycomb cannot be visualized in Figs. 14b and 14d because of the density difference between the aluminium honeycomb and the steel face sheets.

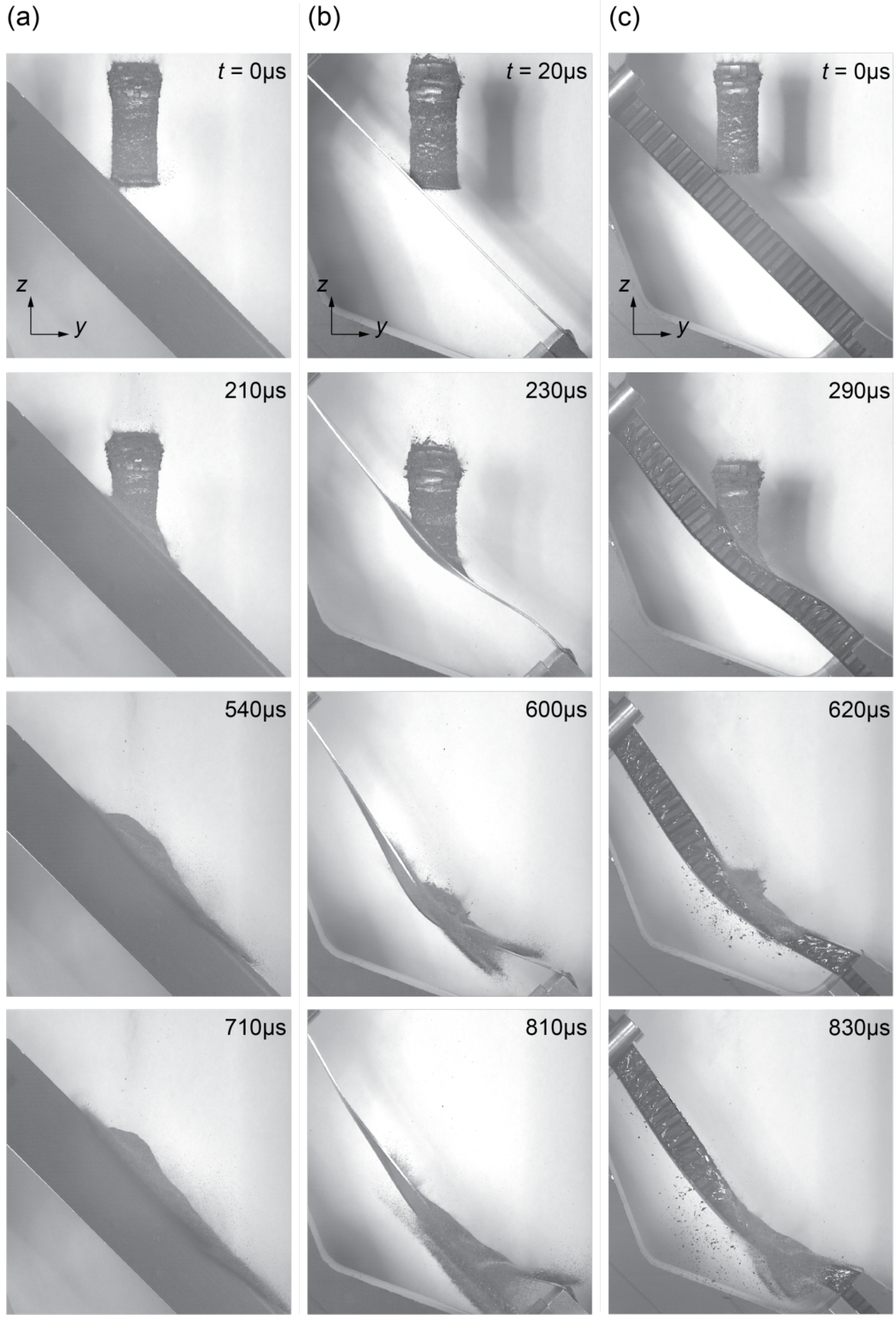

Fig. 12. High-speed images for the slug impact at $v_o \approx 100$ m s^{-1} against the inclined (a) rigid, (b) monolithic and (c) sandwich beams. Each image is marked with a time stamp and time $t = 0$ corresponds to the instant that the slug impacts the beam. The global coordinate system (x, y, z) from Fig. 5 is indicated in the first image of each part.

Next consider the case of the inclined impact. It is clear that for both the monolithic and sandwich beams, the point of maximum deflection is not at mid-span but shifted towards the distal end of the beam as discussed above (Figs. 13c and 13d). The region of core shear in the sandwich beams is also spread over a larger length of the beam compared to the normal impact case. The X-ray images of the beams in Figs. 14c and 14d also show dishing-type deformation for the inclined monolithic and sandwich beams. However, unlike the normal impact case, the core compression is reasonably uniform across the width of the beam at the location where maximum core compression occurs.

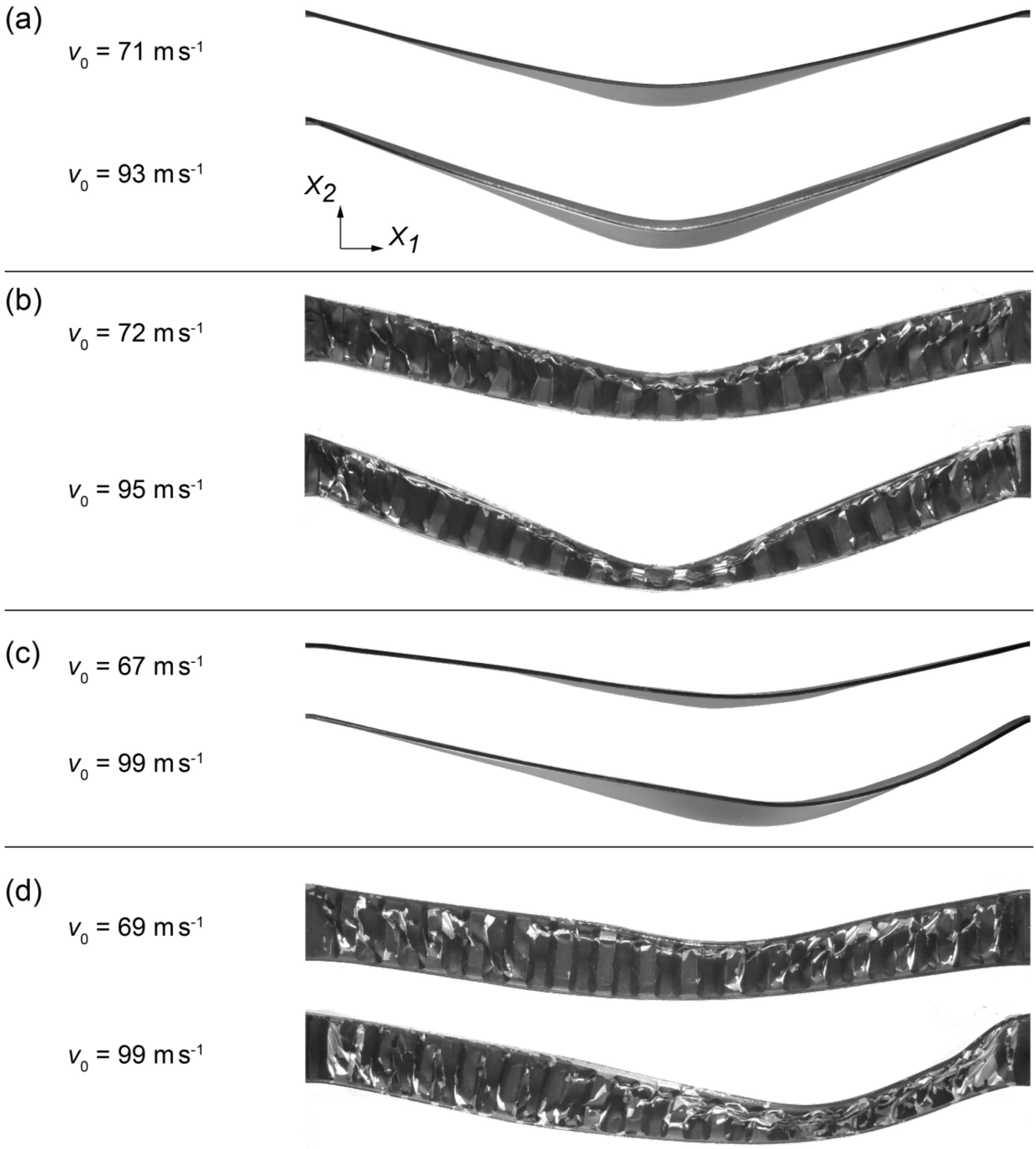

Fig. 13. Photographs of the deformed profiles of the normally oriented (a) monolithic and (b) sandwich beams as well as the inclined (c) monolithic and (d) sandwich beams. Each part includes deformed profiles for two values of the slug velocity v_o. Only the $2\ell = 100$ mm free span of the beams are shown and the coordinate system (X_1, X_2, X_3) from Fig. 3 is indicated.

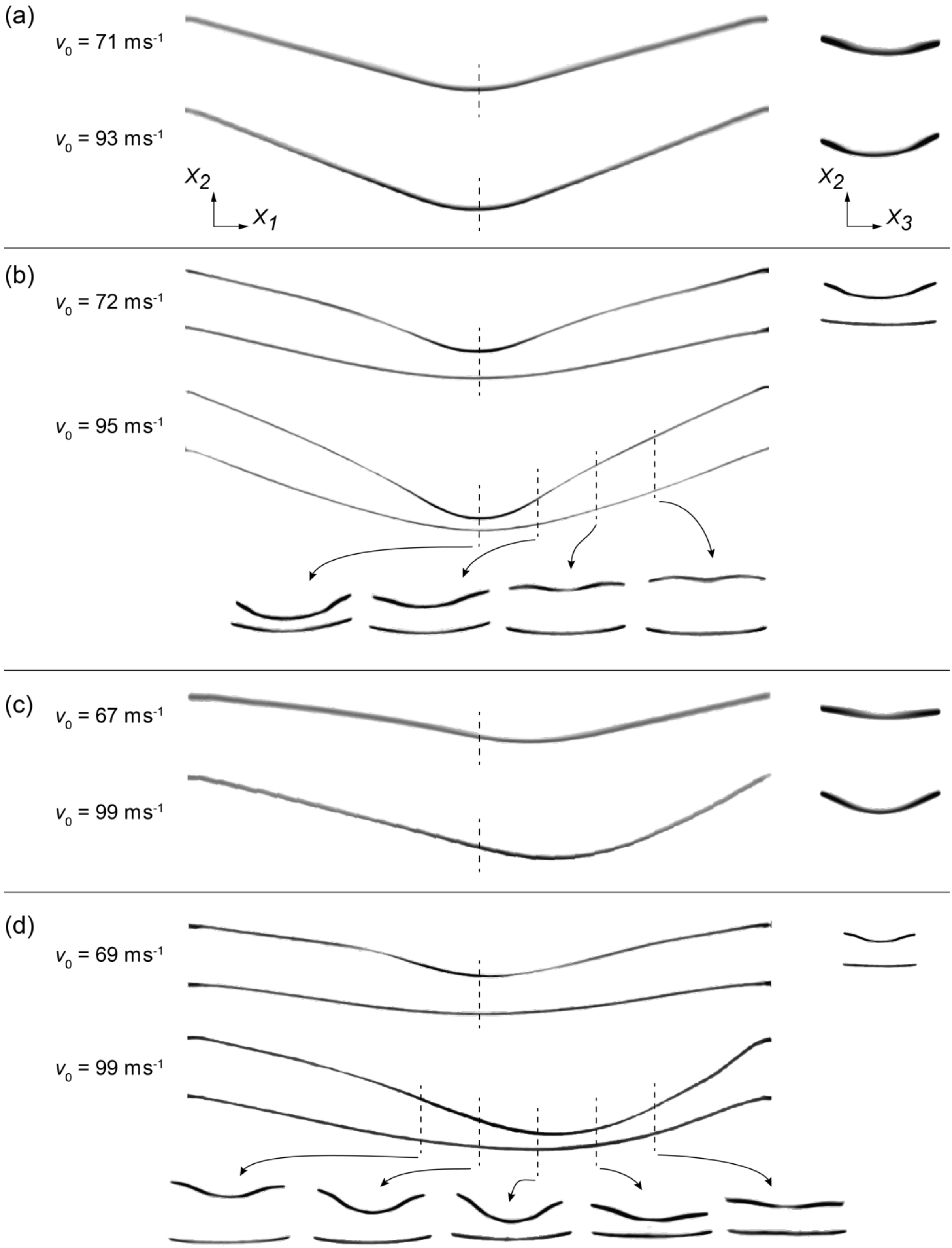

Fig. 14. Section cuts from X-ray computed tomographic scans of the beams from Fig. 13, viz. the normally oriented (a) monolithic and (b) sandwich beams as well as the inclined (c) monolithic and (d) sandwich beams. In each case, a section in the $X_1 - X_2$ plane at mid-width is shown along with a section in the $X_2 - X_3$ plane at mid-span. Additional sections in the $X_2 - X_3$ plane are included in parts (b) and (d) as indicated.

In order to compare the performance of the monolithic and sandwich beams, we define w_{max} as the maximum permanent deflection of the beams, i.e. the maximum deflection measured perpendicular to the undeformed beam. For the normal impact against the monolithic beam, the maximum deflection occurs at the geometrical centre of the beam (mid-width and mid-span). On the other hand, for the inclined case, the location of maximum deflection is not at mid-span but rather translated towards the distal support. For the monolithic beam w_{max} for the back and front faces are almost identical while they differ substantially for the sandwich beams due to core compression. Thus, we report a single value of w_{max} for the monolithic beams but report w_{max} for both the front and back faces of the sandwich beams. These measured values of w_{max} are plotted as a function of v_o in Figs. 15a and 15b for the normal and inclined impact cases, respectively. Over the entire range of v_o, the deflections w_{max} increase approximately linearly with v_o and the back face deflections of the sandwich beams are significantly smaller compared to the corresponding values of the monolithic beams. By comparing Figs. 15a and 15b, it is apparent that inclination of the beams reduces the deflections considerably. In fact, inclination and sandwich construction have approximately the same beneficial effect, i.e. the deflection of the inclined monolithic beam is approximately equal to the back face deflection of the sandwich beam impacted normally at the same slug velocity.

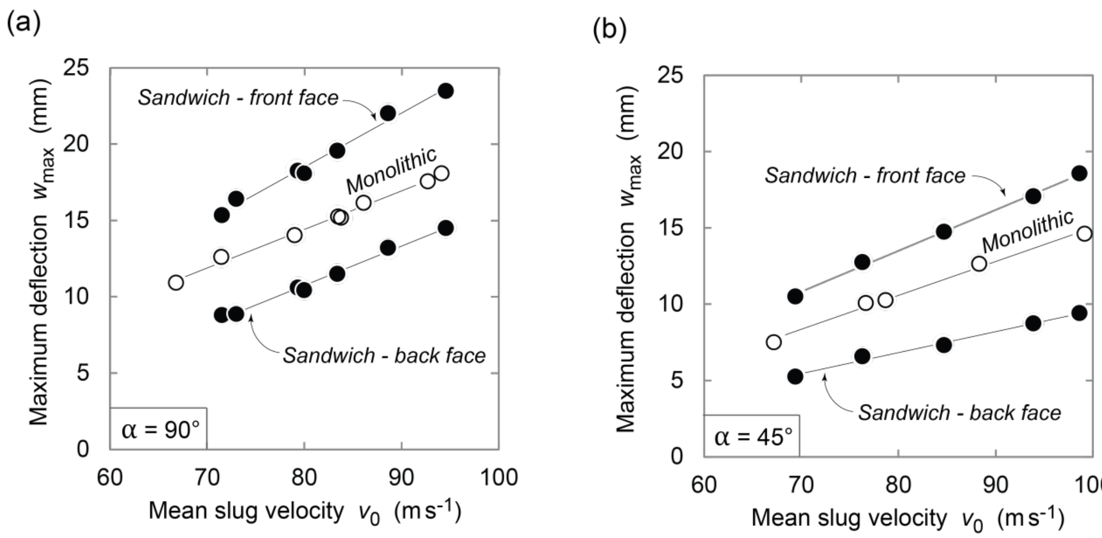

Fig. 15. The measured permanent maximum deflections w_{max} of the monolithic and sandwich beams as a function of the slug velocity v_o for the beams in the (a) normal and (b) inclined orientation. Measurements of the maximum deflections for both the front and back face of the sandwich beams are included.

As discussed above, the benefit of sandwich construction over monolithic construction arises from the higher strength and stiffness of a sandwich beam over the equal mass monolithic beam. On the other hand, the benefit of inclination is typically based on the assumption that for a given free-field slug momentum, less momentum is transmitted into an inclined beam compared to a normally oriented beam. While this is true for rigid beams (Tremblay, 1998), we shall demonstrate in Section 3.2 that the momentum transmitted into the deformable monolithic and sandwich beams can be equal to or greater than the momentum of the incoming slug of WC particles. This is due to fluid-structure interaction effects arising from the diversion of the particle flow by the dynamic deformation of the beams. Here we will thus argue that the main reason for the performance benefit achieved by inclination is associated with the fact that the location of maximum deflection of the inclined beam translates towards one of the supports. This reduces the effective span of the beam, which has two effects: (i) the effective bending strength and stiffness of the beam increases and (ii) the stretching strain induced in a beam for a given deflection w also increases, thereby increasing the effective stretching strength of the beams since the stretching strain in the beam scales as $(w/l_e)^2$ where l_e is the effective half-span of the beam. While both of these effects are in play for both the monolithic and sandwich beams, we anticipate that (i) dominates for the sandwich beams while (ii) is the major effect for monolithic beams.

The maximum core compression strain ε_c^{max} is defined as the maximum value of $\Delta H_c/H_c$ over the entire span of the beam, where ΔH_c is the permanent reduction in the core thickness of the sandwich beam. The measured maximum core compression ε_c^{max} is plotted as a function of v_o in Figs. 16a and 16b for the normal and inclined impact cases, respectively (on the right-hand y-axis). As a consequence of the linear dependence of w_{max} on v_o, the core compression also increases approximately linearly with v_o. Intriguingly, while ε_c^{max} is approximately equal for the inclined and normal impact cases at high values of v_o, ε_c^{max} is significantly lower in the inclined case at the lower end of the v_o range investigated here.

A comparison of the results in Figs. 15a and 15b suggest that inclination combined with sandwich construction seems to have some synergistic effects in the following sense. The w_{max} versus v_o curves for the monolithic and sandwich beams (back face) are approximately parallel for the normal impact case but seem to diverge for the inclined impact case. The beneficial effect of sandwich beams in an inclined impact situation increases with increasing v_o. In order to quantify this effect we perform a linear regression fit of the form $w_{max} = c_1 v_o + c_2$ to the monolithic and sandwich (back face) beam data in Fig. 15. These linear fits are plotted in Fig. 15 and the fitting parameters (c_1, c_2) listed in Table 2. Using these equations, we plot the ratio $\bar{w}$ of the maximum deflections of the sandwich beam to the monolithic beam as a function of v_o in Figs. 16a and 16b for the normal and inclined impact cases, respectively (on the left-hand y-axis). The ratio $\bar{w}$ increases with v_o for the normal impact case showing that the benefit of sandwich construction is reduced with increasing slug velocity. This was also predicted by the simulations of Liu et al. (2013), who rationalised the result by observing that core compression increases with increasing v_o, which in turn reduces the bending strength of the beam and thereby diminishes the beneficial sandwich effect. On the other hand, the plot of $\bar{w}$ versus v_o for the inclined case (Fig. 16b) suggests that the benefit of sandwich construction remains undiminished with increasing slug velocity. While reasons for this are unclear, we speculate that this is a result of translation of the point of maximum deflection towards the support for the inclined impact case: this translation, which reduces the effective span of the beam, seems to have a more significant effect for the sandwich compared to the monolithic beam and helps the sandwich beam to maintain its performance benefit, even under conditions of substantial core compression.

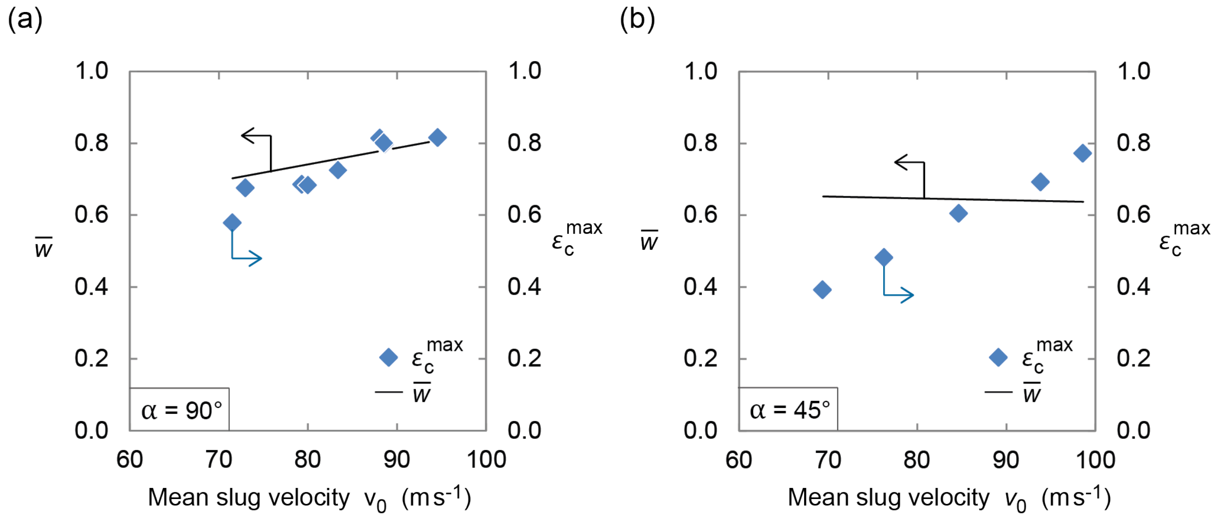

Fig. 16. The maximum core compression ε_c^{max} (right-hand y-axis) and ratio $\bar{w}$ of the maximum deflections of the sandwich beams to the monolithic beams (left-hand y-axis) as a function of the slug velocity v_o for beams in the (a) normal and (b) inclined orientations.

Table 2. The coefficients (c_1, c_2) in the equation $w_{max} = c_1 v_o + c_2$ used to fit the measurements of the maximum deflections of the monolithic and sandwich beams in Fig. 15.

Beam type	α (°)	c_1 (μs)	c_2 (mm)
Sandwich	90	257.9	9.2
	45	137.2	4.1
Monolithic	90	252.8	5.8
	45	221.9	7.2

3.2 Characterisation of the transmitted momentum

The dynamic deformation of the monolithic and sandwich beams causes flow reversal (Figs. 10 and 12) and so the ratio of the momentum transferred into these deforming structures to the incoming free-field momentum of the slug is anticipated to be a function of both deformation and impact velocity. While predictions of strong “fluid-structure” interaction effects have been reported (Liu et al., 2013; Wadley et al., 2013), there are no measurements available in the open literature. Here we present measurements of the momentum transferred into the beams under normal and inclined impact conditions in order to quantify this fluid-structure interaction effect.

Reference measurements of momentum transfer

Recall that the beam support rigs for the normal and inclined impact are placed on two three-component piezoelectric force transducers. The force versus time histories measured from these transducers will enable us to estimate the momentum transferred into the beams in each of the three orthogonal directions (x, y, z), see Fig. 5. Numerical calculations reported by

Liang et al. (2007) and Tilbrook et al. (2006) suggest that the transmitted force versus time histories are very strongly dependent on: (i) the precise location within the support structure at which the measurements are made, (ii) the structural properties of the support structure (e.g. its stiffness and mass), and (iii) the details of the clamping set-up (e.g. the stiffness of the bolts, friction between the clamping plates and beams, etc.). It is thus not insightful to try and analyse these transmitted force versus time histories. By contrast, the integral of the force versus time histories is not as dependent on the support structure, but instead are mainly dependent on the impacting granular material and the deformation of the beam. Thus, in this study we focus only on this integral quantity, viz. the transmitted momentum.

In order to gauge the accuracy of our measurement system, we first report momentum measurements for the normal and inclined impact against the rigid beams. For these rigid beams, analytical expressions can be derived to relate the incoming to the transmitted momentum. Sketches of the normal and inclined impact of the slug against rigid and stationary surfaces are shown in Figs. 17a and 17b, respectively. Motivated by the high-speed photographic observations in Figs. 10a and 12a, the sketches illustrate that the WC slugs spread over the surface and do not bounce off the surface. Moreover, for the inclined case the spreading of the slug is asymmetrical such that the momentum I_1 of the particles flowing in the positive z-direction is different from I_2 of the particles flowing in the negative z-direction. Applying momentum conservation in the z- and y-directions gives:

$$I_0 - I_t^z - \cos\alpha\, I_1 + \cos\alpha\, I_2 = 0 \tag{3.1}$$

and

$$I_t^y - \sin\alpha\, I_1 + \sin\alpha\, I_2 = 0, \tag{3.2}$$

where we have used the notation of Fig. 17b: I_o is the free-field momentum of the incoming slug in the negative z-direction; I_t^z and I_t^y are the reaction momenta exerted by the supports on the rigid surface in the z- and y-directions, respectively (we refer to these as the transmitted momenta). Recalling that for the case of normal impact ($\alpha = 90°$), the spreading is symmetric and so $I_1 = I_2$. Thus

$$I_t^y = 0 \quad \text{and} \quad I_0 = I_t^z. \tag{3.3}$$

On the other hand, for the inclined case, I_1 and I_2 are both unknown. Thus, we are unable to separately estimate I_t^z and I_t^y from just Eqs. (3.1) and (3.2). However, $\sin\alpha = \cos\alpha$ for the special case of $\alpha = 45°$ and this simplifies the Eqs. (3.1) and (3.2) such that

$$I_0 = I_t^z + I_t^y. \tag{3.4}$$

Equation (3.4) along with Eq. (3.3) can be used to gauge the accuracy of our experimental set-up used to measure the momentum transmitted by the impact of WC slugs against rigid beams in the normal and inclined orientation.

The two force transducers provide measurements of force versus time histories in the x-, y- and z-directions. We will label the force measured by transducer 1 and 2 in the z-direction as F_z^1 and F_z^2, respectively. Consequently, the momentum i_t^z transmitted into the support structure in the z-direction after time t (where $t = 0$ corresponds to the instant that the slug impacts the beam) is given by

$$i_t^z(t) = \int_0^t (F_z^1 + F_z^2)dt, \tag{3.5}$$

and $I_t^z \equiv i_t^z(t \to \infty)$. Analogous expressions exist for the momenta in the other directions, viz. I_t^y and i_t^y as well as I_t^x and i_t^x. In all experiments, $i_t^x = 0$ to within the accuracy of the measurements and hence the focus is on the momentum measurements in the z- and y-direction.

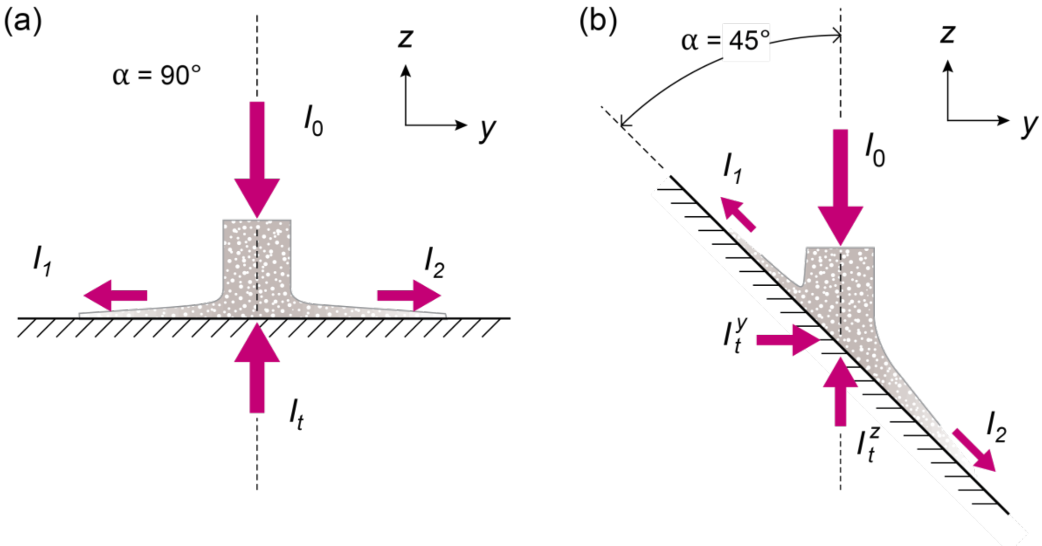

Fig. 17. Sketches of the impact of a WC slug against a rigid and stationary target in the (a) normal and (b) inclined orientation. The global coordinate system (x, y, z) is indicated and the components of the transmitted momentum in the different directions are labeled.

Let us now consider the case of slug impact at $v_o \approx 95$ m s^{-1} against the rigid beam in the normal and inclined orientation at a stand-off $S = 110$ mm. Measurements of i_t^z/I_o are reported in Fig. 18a for the normal impact, while both i_t^z/I_o and i_t^y/I_o are reported in Fig. 18b for the inclined case ($i_t^y/I_o \approx 0$ for the normal impact and hence not reported here). After a small initial time lag (corresponding to the time taken for the stress waves initiated at the impact location to reach the force transducers), the momentum rises sharply and subsequently oscillates about a fixed mean value. We observe that the amplitude and period of the oscillations are smaller for the inclined case as compared to the normal case. These oscillations are related to the natural frequency of the entire set-up, which depends on the mass and stiffness of the test set-up (the mass of the support rig used in the inclined case is less than that used for the normal impact case). Based on these observations we use the following working definitions for I_t^z and I_t^y:

(i) for the normal impact case, we define I_t^z as the average value of i_t^z between the second and third peak of the oscillations in the i_t^z versus t curve;

(ii) for the inclined impact case, I_t^z is defined as the average value of i_t^z over the period 2.5 ms $\leq t \leq$ 3.5 ms (again an analogous definition is used for I_t^y).

The values of I_t^z and I_t^y (as defined above) normalized by the free-field momentum of the slug I_o are plotted in Fig. 19 as a function of the slug velocity v_o for both normal and inclined impacts against the rigid beam. Also included in Fig. 19 is the normalized sum $(I_t^z+I_t^y)/I_o$ for the inclined beam. With $I_t^z/I_o = 1.05$ for the normal and $(I_t^z+I_t^y)/I_o = 1.06$ for the inclined impact, it is clear that our measurements are in line with Eqs. (3.3) and (3.4), respectively. This not only confirms the fidelity of the measurement system but also gives additional insight with regards to the momentum transmitted into an inclined rigid structure by the WC slug.

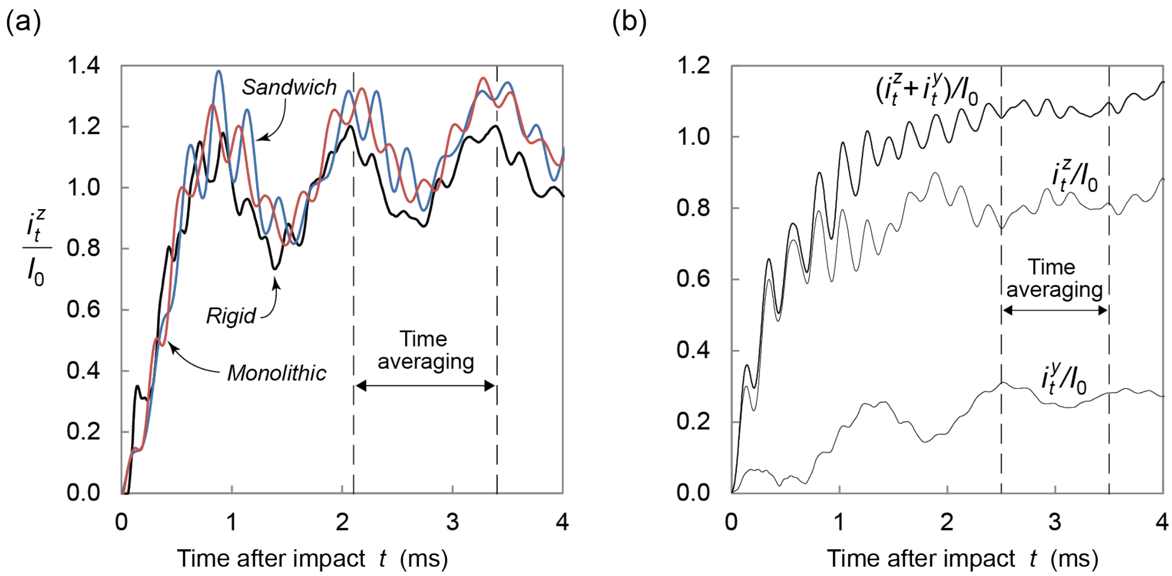

Fig. 18. Measurements of the normalized transferred momentum i_t^z/I_o and i_t^y/I_o as a function of time t for the (a) normal and (b) inclined impact cases. Time $t = 0$ corresponds to the instant that the slug impacts the beam and results are shown for the slug impact at $v_o \approx 95$ m s^{-1}. In part (a), measurements for the rigid, monolithic and sandwich beams are included, while in part (b), results are only shown for the rigid beam.

Neglecting friction between the flowing fluid and structure as well as any rebound of the fluid, the momentum transmitted into a rigid inclined structure by the impact of a slug is given by (see Appendix B for a detailed derivation)

$$I_t^y/I_0 = \cos\alpha \, \sin\alpha \, , \tag{3.6}$$

and

$$I_t^z/I_0 = \sin^2 \alpha. \tag{3.7}$$

This implies that for, say, a water slug impacting a rigid surface inclined at $\alpha = 45°$, $I_t^z/I_0 = I_t^y/I_0 = 0.5$ and the resultant transmitted momentum is given by

$$I_t = \sqrt{(I_t^z)^2 + \left(I_t^y\right)^2}, \tag{3.8}$$

since ($I_t^x = 0$). Thus, $I_t/I_0 = 0.71$ for the impact of an inviscid slug against an rigid surface inclined at $\alpha = 45°$. By contrast, for the WC slugs, $I_t^y/I_0 \approx 0.28$ and $I_t^z/I_0 \approx 0.79$ with $I_t/I_0 \approx 0.83$, i.e. the momentum transfer due to the impact of the WC slug against a rigid inclined target clearly results in higher levels of momentum transfer compared to impact of an inviscid, incompressible fluid. Since neither the Bernoulli principle nor the incompressibility constraint are directly applicable to the impact of the WC slug, we anticipate that the momentum transmitted into the inclined target depends on the constitutive response of the WC slug. By contrast, the symmetry of the normal impact situation implies that the momentum transfer due to the normal impact of the WC slug and the inviscid incompressible fluid result in identical levels of momentum transfer, i.e. $I_t^y/I_0 = 0$ and $I_t^z/I_0 = I_t/I_0 = 1$. We thus conclude that the inviscid, incompressible fluid analogy used to analyse the impact of sand against a target may not be appropriate for an inclined plate.

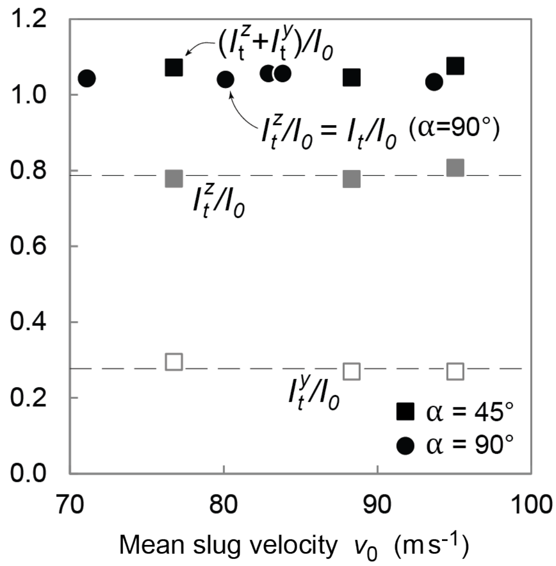

Fig. 19. The normalized transmitted momentum I_t^z/I_o and I_t^y/I_o for the inclined rigid beams as well as I_t^z/I_o for the normally oriented rigid beams as a function of the slug velocity v_o. Dashed lines indicate the mean value of the measurements for I_t^z/I_o and I_t^y/I_o. The normalized sum $(I_t^z+I_t^y)/I_o$ is also included for the inclined rigid beams.

Monolithic and sandwich beams

Measurements of i_t^z/I_o versus t are included in Fig. 18a for the normal impact of WC slugs against the monolithic and sandwich beams for $v_o \approx 95$ m s^{-1}. It is clear that the period and amplitude of the oscillations are approximately the same for the rigid, monolithic and sandwich beams, confirming that these oscillations are not due to the deformation of the test structure but rather related to the vibration response of the support structure. Thus, it is acceptable to use the same definitions of I_t^z and I_t^y as detailed above for the rigid beams to analyse the momentum transfer for the deformable monolithic and sandwich beams as well.

First consider the normal impact of the monolithic and sandwich beams. Measurements of I_t^z/I_o are included in Fig. 20 for the monolithic and sandwich beams over the whole range of slug velocities investigated here (since $I_t^y = 0$, the resultant transferred momentum $I_t = I_t^z$ for the normal impact case). The dashed horizontal line in Fig. 20 gives the average value from the rigid beam measurements in Fig. 19. Consistent with the predictions of Liu et al. (2013), the measurements here indicate that the momentum transferred into the monolithic and sandwich beams by a normal slug impact is between 10-20% greater than that transmitted into the rigid beam. Moreover, to within the accuracy of the measurement system used here, the momentum transmitted into the monolithic beam is equal to that transmitted into the sandwich beam. These results thus support the findings of Liu et al. (2013) that fluid-structure interaction effects play a relatively minor role during impact of particle slugs against normally oriented monolithic and sandwich beams.

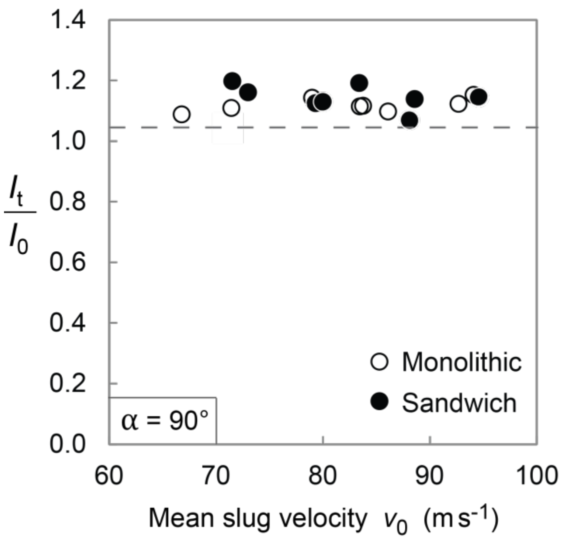

Fig. 20. The normalized transmitted resultant momentum $I_t^z/I_o = I_t/I_o$ for the normal impact against the monolithic and sandwich beams as a function of the slug velocity v_o. The dashed line is the average value from Fig. 19 for the normal impact against the rigid beam.

Next consider the inclined impact case. Measurements of I_t^z/I_o and I_t^y/I_o as a function of v_o are included in Figs. 21a and 21b for both the monolithic and sandwich beams, respectively. A larger fraction of the incoming momentum is transmitted in the z-direction and this fraction increases with increasing v_o. Simultaneously, the fraction I_t^y/I_o decreases with increasing v_o. Moreover, both components of the transmitted momentum are approximately the same for the monolithic and sandwich beams at the same value of v_o. We now proceed to quantify the resultant transmitted momentum for these inclined, deformable beams and compare their values with those of the rigid beam.

Recall that the resultant transmitted momentum is given by Eq. (3.8) and this transmitted momentum vector makes an angle

$$\theta = \tan^{-1}\left(\frac{I_t^y}{I_t^z}\right) \tag{3.9}$$

with the z-axis. The resultant momentum transmitted into the rigid beam is $I_t^{rigid} \approx 0.83 I_o$ for all values of v_o. Unlike the normal impact case, only 83% of the incoming momentum is transmitted into the structure since the WC particle retain a residual velocity in the negative z-direction after the impact event. The ratio I_t/I_t^{rigid} and θ as a function of v_o are plotted in Figs. 22a and 22b, respectively, for the monolithic and sandwich beams. The key observations are:

(i) Consistent with the momentum component data in Fig. 21, the resultant transmitted momentum plotted in Fig. 22 is the same for the monolithic and sandwich beams.

(ii) The angle θ of the resultant transmitted momentum decreases with increasing v_o, i.e. a larger fraction of the incoming momentum is transmitted in the z-direction.

(iii) Unlike the normal impact case, the resultant momentum transmitted into the inclined deformable beams (monolithic and sandwich) is much larger than that transmitted into the inclined rigid beam. Moreover, I_t/I_t^{rigid} increases approximately linearly with increasing v_o.

(iv) Measurements reported in the literature (e.g. Pickering et al. 2013) only measure the z-component of the transmitted momentum using a ballistic pendulum. Thus, the measurements typically underestimate the resultant momentum transmitted – the measurements reported here show that a significant fraction of the momentum is transmitted in the y-direction.

The normalized transmitted momentum $I_t/I_o = 0.83 I_t/I_t^{rigid}$ is indicated on the right-hand y-axis of Fig. 22a. This highlights that over the range of the slug velocities investigated here, the momentum transmitted into the inclined deformable beams is equal to or greater than the incoming slug momentum. This is due to the fluid-structure interaction effect discussed above and only recognised when all components of the momentum are measured as done in this study. Thus, as alluded to in Section 3.1, we argue that the reduction in the deflections of the inclined beams compared to the normally oriented beams is primarily a result of the translation of the point of maximum deflection towards the support, rather than due to a smaller momentum being transmitted into the inclined beams.

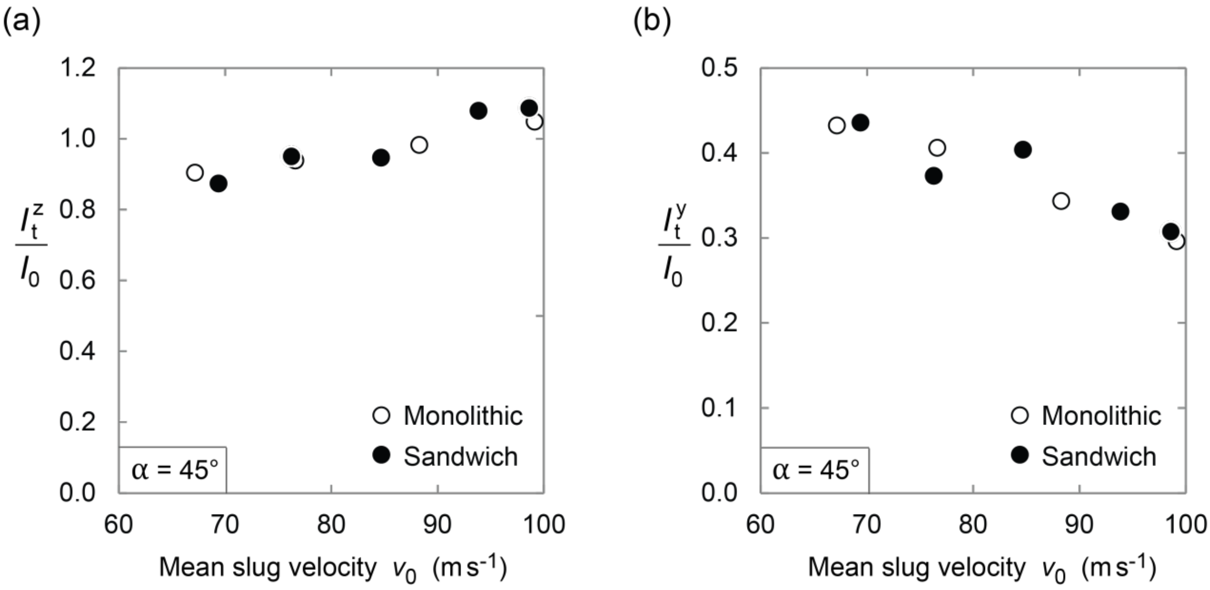

Fig. 21. The normalized transmitted momentum (a) I_t^z/I_o and (b) I_t^y/I_o as a function of the slug velocity v_o for the impact against the inclined monolithic and sandwich beams.

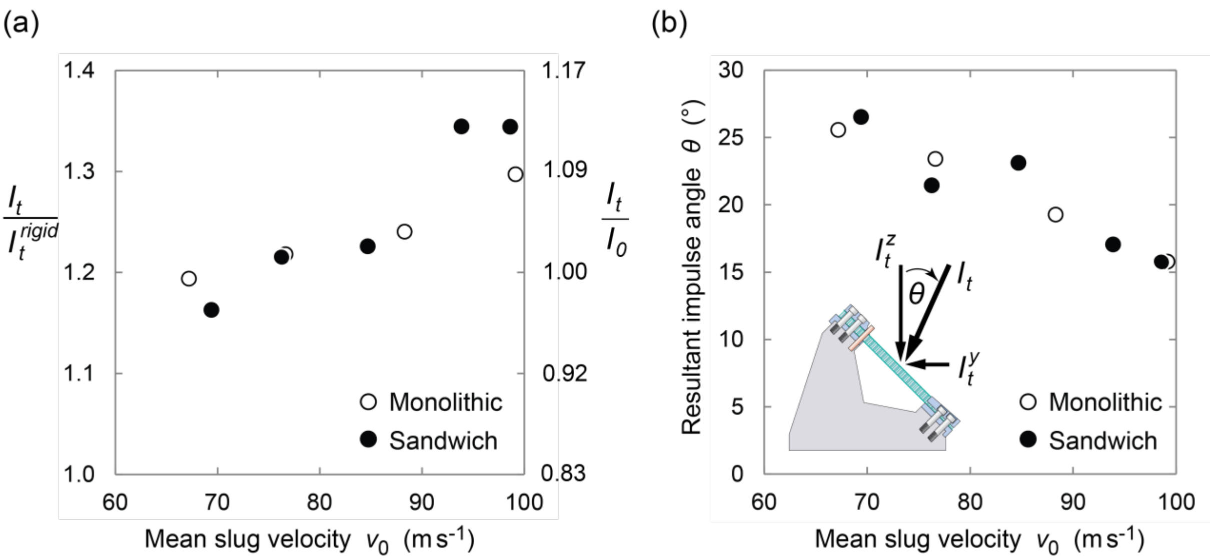

Fig. 22. (a) The normalized resultant transmitted momentum I_t/I_o (right-hand y-axis) and I_t/I_t^{rigid} (left-hand y-axis) for the inclined impact case. (b) The direction θ of this resultant as a function of the slug velocity v_o for the impact against the inclined monolithic and sandwich beams. The inset in part (b) shows a sketch of the components of the transmitted momentum and the definition of θ.

4 Effect of stand-off on the response of the beams

The simulations of Liu et al. (2013) have suggested that only two loading parameters govern the response of beams impacted by granular slugs, namely the free-field momentum of the slugs and the loading time. To first order, the loading time τ of the slugs is given by

$\tau \approx L_s/v_0$, where L_s is the length of the slug at the instant of impact. Recall from Fig. 7a that there is a spatial gradient in the axial particle velocity within the slugs such that the front of the slug is moving faster than the rear. Thus, the length L of the slug is increasing as it travels towards the target and consequently L_s increases with increasing stand-off S. Given that the velocities of the slugs prior to impact are temporally invariant, this implies that for a given slug velocity v_0, the loading time τ increases while the free-field slug momentum remains constant with increasing S. The simulations of Liu et al. (2013) would then suggest that the beam deflections decrease with increasing S.

In order to investigate this prediction we performed normal impact tests on the monolithic and sandwich beams with a smaller stand-off of $S = 65$ mm over the same slug velocity range as for the measurements with $S = 110$ mm reported above. The maximum permanent deflections w_{max} of the monolithic and back face of the sandwich beams are plotted in Fig. 23 as function of the slug velocity v_0 for both the $S = 65$ mm and 110 mm stand-off. It is clear that for a given v_0, w_{max} is higher for the $S = 65$ mm compared to the $S = 110$ mm case for both the monolithic and sandwich beams. Interestingly, for the stand-offs considered here, the sandwich beam at the $S = 65$ mm stand-off outperforms the monolithic beam at the $S = 110$ mm stand-off, i.e. the performance benefit of sandwich construction outweighs that for stand-off for the parameters investigated here. However, no synergistic effects are observed between increasing stand-off and sandwich construction with all the w_{max} versus v_0 curves being parallel in Fig. 23.

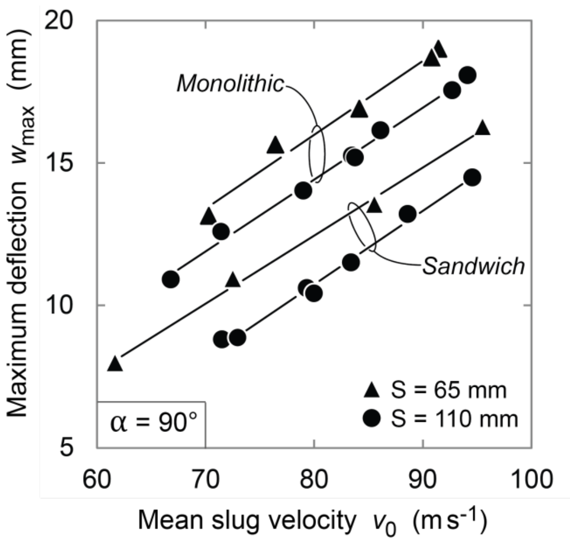

Fig. 23. The measured permanent maximum deflections w_{max} of the monolithic and sandwich beams as a function of the slug velocity v_o for the normally oriented beams. Measurements are shown for two values of the stand-off S and only include the back face deflections of the sandwich beams.

5 Concluding remarks

The dynamic response of end-clamped sandwich and monolithic beams subjected to high-velocity impact (60 m s^{-1} $-$ 100 m s^{-1}) of slugs comprising tungsten carbide (WC) particles was experimentally investigated. The monolithic beams were made from AISI 304 stainless steel, while the sandwich beams of equal areal mass comprised face sheets of the same stainless steel and an aluminium honeycomb core.

High-speed imaging was used to study the effect of beam inclination and stand-off on their dynamic deformation, and three-component load measurements were used to quantify the momentum transmitted by the beams into the support structure. Tests were also performed on nominally rigid beams, which served as a baseline to delineate the effects arising from the interaction of the impacting slug and the dynamically deforming beams. The main findings of the study are:

- Sandwich beams in both the normal and inclined orientations undergo significantly smaller back face deflections compared to their monolithic counterparts.
- In the normal impact case, the ratio of the maximum back face deflection of the sandwich and monolithic beams increases with increasing slug impact velocity. However, in the inclined orientation, this ratio remains constant over the entire range of impact velocities investigated, i.e. combining inclination with sandwich construction seems to give synergistic effects.
- During normal impacts, the momentum transmitted into the support structure is approximately equal to the incoming momentum of the slug over the entire range of slug velocities for monolithic and sandwich beams (as well as the rigid beams). By contrast, the ratio of the transmitted to incoming momentum increases with increasing slug velocity for the inclined sandwich and monolithic beams but remains fixed at approximately 83% of the incoming momentum for the rigid beams. Intriguingly, the momentum transmitted into the deformable inclined monolithic and sandwich beams was always equal to or greater than the incoming slug momentum.
- The reduction in the deflections of the inclined beams compared to their normally oriented counterparts is attributed to the fact that the location of maximum deflection translates towards the supports, which in turn increases the effective bending and stretching strength of the beams. Thus, while we observe clear benefits of inclined beams over their normally oriented counterparts, we argue that this benefit is not due to a reduction in the transmitted momentum as widely assumed.
- Increasing the beam stand-off reduces the deflections of both the monolithic and sandwich beams. However, unlike the case of inclination, there is no synergistic effect when combining increased stand-off with sandwich construction.

Appendix A

The static properties of the sandwich beam constituent materials and the WC slugs

Solid 304 stainless steel sheets: Two thicknesses (0.3 mm and 0.7 mm) of AISI 304 stainless steel sheets were used for the manufacture of the sandwich and monolithic beams investigated here. Tensile specimens of dog-bone geometry were cut from each of the as-received stainless steel sheets and subsequently the 0.3 mm specimens were subjected to the same heating cycle as used to cure the sandwich beams. The uniaxial tensile responses of the two sheet thicknesses at an applied strain-rate of 10^{-4}s^{-1} are plotted in Fig. A.1a. The yield strengths of the 304 stainless steel sheets are in the range 265 to 292 MPa and both sheets exhibit approximately linear strain hardening. The impact tests reported here suggest that the high strain response of AISI304 stainless steel is important in these situations. This high strain rate behaviour of AISI304 stainless steel has been measured by Stout and Follansbee (1986) and used in FE calculations of impact of sandwich structures (at velocities similar to those employed here) by Rubino et al. (2008). These calculations showed that to within a very good first approximation the quasi-static response of the steel suffices in capturing the dynamic observations.

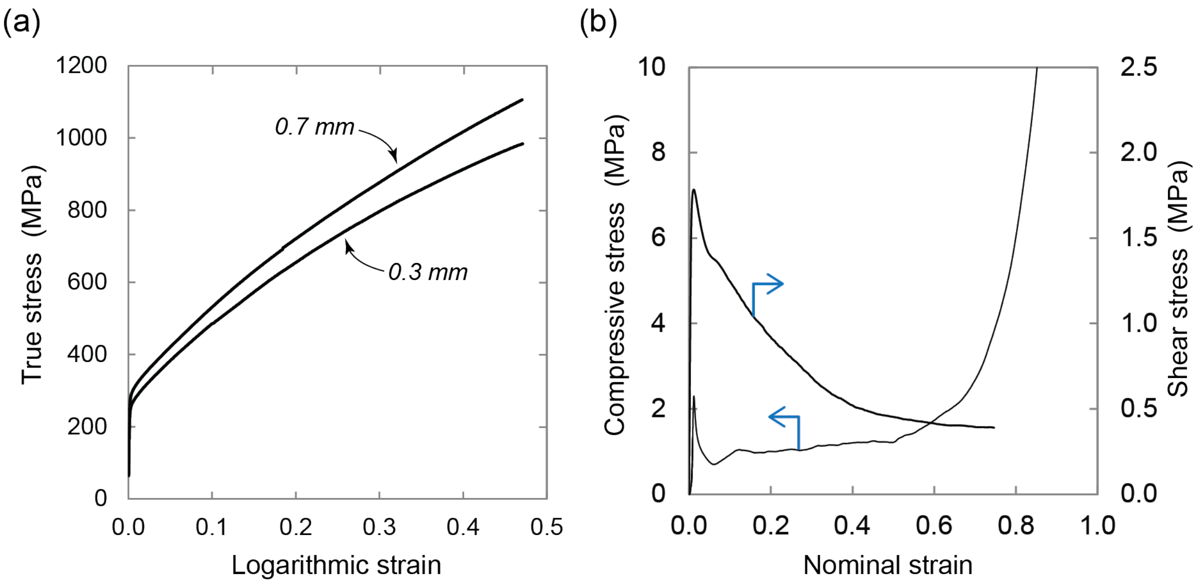

Fig. A.1. Measured quasi-static tensile response of AISI 304 stainless steel sheets for two thicknesses; 0.7 mm thick sheets were used for the monolithic beams, while 0.3 mm sheets were used for the face sheets of the sandwich beams. (b) Measured quasi-static compressive and shear response of the aluminum honeycomb used to manufacture the sandwich beams.

Compressive and shear responses of the Al honeycomb: We describe the quasi-static compressive and shear response of the Al honeycomb cores with reference to the coordinate system sketched in Fig. 3. The uniaxial compression experiments to measure the $\sigma_{22} - \varepsilon_{22}$ response of the $H_c = 10.3$ mm honeycomb cores were conducted at an applied compressive strain rate of 10^{-3}s^{-1}. The specimens comprised 6x6 cells and as for the sandwich beams, the honeycomb cores were bonded to 0.3 mm thick stainless steel sheets using the same curing cycle. The specimens were compressed between parallel hardened steel platens in a screw-driven load frame. The measured nominal compressive stress σ_{22} versus nominal compressive strain ε_{22} response is included in Fig. A.1b. Consistent with a wide body of data, compression in the out-of-plane direction results in a high initial peak stress followed by a plateau stress where the honeycomb progressively crushes. The compressive stress then rises rapidly at strains in excess of about 60% when densification of the honeycomb sets in.

The out-of-plane shear response $\tau_{12} - \gamma_{12}$ was measured according to ASTM C 273 (2007) using a single-lap shear set-up. The honeycomb was bonded between two 24 mm thick Al alloy plates using Redux 312L and the same curing cycle as employed for the sandwich beams. The shear response measured at an applied strain rate of 10^{-3} s^{-1} is included in Fig. A.1b: following an initial elastic response, the honeycombs exhibit a peak strength followed by a softening response associated with buckling of the cell walls (Zhang and Ashby, 1992).

Confined compressive response of the WC slug: For the sake of completeness we performed confined uniaxial compression tests on the WC slugs. These measurements provide insight into the properties of the aggregate of WC particles and can be used to calibrate the inter-particle contact properties as required in discrete particle calculations such as those in Liu et al. (2013) and Børvik et al. (2011). The set-up comprised a cylinder of mild steel with an outer diameter of 50 mm and an inner diameter of 12.7 mm as well as a double-piston arrangement as shown in the Fig. A.2a. The pistons were made from silver steel (BS-1407) and applied the compressive load to the slugs of initial length 20 mm. The WC slugs were prepared in this cylindrical cavity as described in Section 2.2. Samples with and without the tracer sand particles were prepared in order to investigate the effect of the tracer particles on the compressive response of the slug.

The compressive response of the WC slugs was measured in a screw-driven test machine at an applied strain rate of 10^{-3}s^{-1}. The applied load was measured via the load cell of the test machine, while the relative displacement of the pistons was measured via a laser extensometer. Unloading-reloading cycles were also conducted in order to gauge the level of inelasticity in the compressive response of the slug. The axial stress σ versus nominal strain ε responses of the WC slugs (with and without the tracer sand particles) are plotted in Fig. A.2b, where σ is defined as the ratio of the load applied by the pistons to the cross-sectional area of the slug and ε as the ratio of the relative approach of the pistons to the initial length of the slug. The applied stress was constrained to σ < 300 MPa as the cylinder and piston yielded above this level of stress. After some initial compaction, the response of the WC slug was approximately linear with a hardening rate of approximately 3 GPa. The unloading-reloading cycles conducted after the initial loading to $\sigma = 300$ MPa show that most of the applied strain is irrecoverable and the unloading modulus is approximately 44 GPa. Further the measurements demonstrated that the tracer sand particles have a negligible influence on the $\sigma - \varepsilon$ response of the slug.

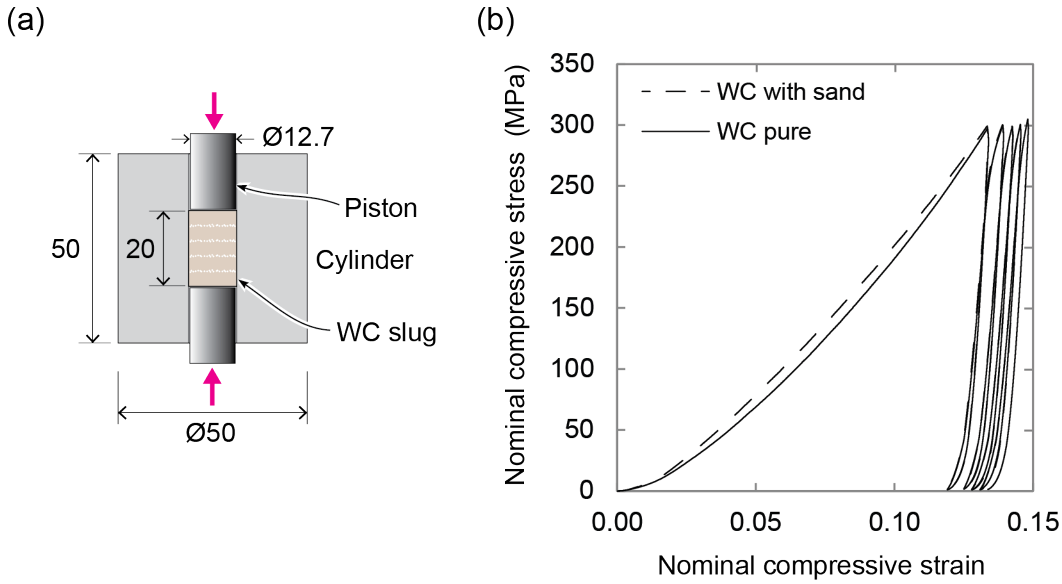

Fig. A.2. (a) Sketch of the double-piston arrangement used to study the quasi-static compressive response of WC slugs. All dimensions are in mm. (b) The measured uniaxial straining response of the WC slugs with and without the tracer sand particles. Loading/unloading traces for the WC slug without the tracer particles are included.

Appendix B

Derivation of the momentum transmitted into a rigid inclined structure.

Here we derive Eqs. (3.6) and (3.7) given above. Consider the case of a slug impacting a rigid inclined structure as shown in Fig. 17b. We neglect any friction between the fluid and the structure as the fluid flows over the structure and use the notation of Fig. 17b. Define a set of axes perpendicular and parallel to the inclined surface denoted by z' and y', respectively. Since the fluid after impact has no velocity perpendicular to the inclined surface, momentum conservation specifies that the transmitted momentum $I_t^{z'} = I_0 \sin\alpha$ and $I_t^{y'} = 0$ since we neglect friction between the surface and the fluid. Resolving the vector components $I_t^{z'}$ and $I_t^{y'}$ into the directions z and y of Fig. 17b directly gives Eqs. (3.6) and (3.7).

Acknowledgments

The work was supported by the Office of Naval Research Grant N00014-09-1-0573 (Program manager, Dr. David Shifler) and the Defense Advanced Projects Agency under grant number W91CRB-11-1-0005 (Program manager, Dr. J. Goldwasser).

References

Anderson, C.E., Behner, T., Weiss, C.E., 2011. Mine blast loading experiments. Int. J. Impact Eng. 38, 697–706.

ASTM Int., 2007. Standard Test Method for Shear Properties of Sandwich Core Materials. Annu. B. ASTM Stand. i, 1–7.

Benedetti, R.E., 2008. Mitigation of Explosive Blast Effects on Vehicle Floorboard, Master thesis, University of Maryland, College Park, MD, USA. University of Maryland.

Bergeron, D., Tremblay, J., 2000. Canadian Research to Characterise Mine Blast Output. 16th Int. MABS Symp.

Bergeron, D., Walker, R., Coffey, C., 1998. Detonation of 100-gram anti-personnel mine surrogate charges in sand, Suffield Report No. 668, Defence Research Establishment, Suffield, Canada.

Børvik, T., Olovsson, L., Hanssen, A.G., Dharmasena, K.P., Hansson, H., Wadley, H.N.G., 2011. A discrete particle approach to simulate the combined effect of blast and sand impact loading of steel plates. J. Mech. Phys. Solids 59, 940–958.

Cheng, X., Varas, G., Citron, D., Jaeger, H., Nagel, S., 2007. Collective Behavior in a Granular Jet: Emergence of a Liquid with Zero Surface Tension. Phys. Rev. Lett. 99, 188001.

Deshpande, V.S., McMeeking, R.M., Wadley, H.N.G., Evans, A.G., 2009. Constitutive model for predicting dynamic interactions between soil ejecta and structural panels. J. Mech. Phys. Solids 57, 1139–1164.

Dharmasena, K.P., Wadley, H.N.G., Liu, T., Deshpande, V.S., 2013. The dynamic response of edge clamped plates loaded by spherically expanding sand shells. Int. J. Impact Eng. 62, 182–195.

Dharmasena, K.P., Wadley, H.N.G., Williams, K., Xue, Z., Hutchinson, J.W., 2011. Response of metallic pyramidal lattice core sandwich panels to high intensity impulsive loading in air. Int. J. Impact Eng. 38, 275–289.

Dharmasena, K.P., Wadley, H.N.G., Xue, Z., Hutchinson, J.W., 2008. Mechanical response of metallic honeycomb sandwich panel structures to high-intensity dynamic loading. Int. J. Impact Eng. 35, 1063–1074.

Fairlie, G., Bergeron, D., 2002. Numerical simulation of mine blast loading on structures, in: 17th Military Aspects of Blast Symposium. Las Vegas, Nevade, pp. 2–9.

Fleck, N.A., Deshpande, V.S., 2004. The Resistance of Clamped Sandwich Beams to Shock Loading. J. Appl. Mech. 71, 386.

Follett, S., 2011. Blast analysis of composite V-shaped hulls: an experimental and numerical approach, PhD thesis, Cranfield University, UK.

Fourney, W., Leiste, U., Bonenberger, R., Goodings, D., 2005. Explosive impulse on plates. Fragblast 9, 1–17.

Fox, D.M., Huang, X., Jung, D., Fourney, W.L., Leiste, U., Lee, J.S., 2011. The response of small scale rigid targets to shallow buried explosive detonations. Int. J. Impact Eng. 38, 882–891.

Genson, K., Foruney, W.L., Taylor, L. 2008. The Effect of Angled Bottoms on the Impulse Delivered to Armored Vehicles, International Journal on Blasting and Fragmentation, 2008, 2, 54-69.

Hlady, S., 2004. Effect of soil parameters on landmine blast, in: 18th Military Aspects of Blast and Shock (MABS) Conference. Bad Reichenhall, Germany.

Johnson, C.G., Gray, J.M.N.T., 2011. Granular jets and hydraulic jumps on an inclined plane. J. Fluid Mech. 675, 87–116.

Kambouchev, N., Radovitzky, R., Noels, L., 2007. Fluid–Structure Interaction Effects in the Dynamic Response of Free-Standing Plates to Uniform Shock Loading. J. Appl. Mech. 74, 1042.

Liang, Y., Spuskanyuk, A. V., Flores, S.E., Hayhurst, D.R., Hutchinson, J.W., McMeeking, R.M., Evans, A.G., 2007. The Response of Metallic Sandwich Panels to Water Blast. J. Appl. Mech. 74, 81.

Liu, T., Fleck, N.A., Wadley, H.N.G., Deshpande, V.S., 2013. The impact of sand slugs against beams and plates: Coupled discrete particle/finite element simulations. J. Mech. Phys. Solids 61, 1798–1821.

McShane, G.J., Deshpande, V.S., Fleck, N.A., 2013. A laboratory-scale buried charge simulator. Int. J. Impact Eng. 62, 210–218.

Morris, B.L., 1993. Analysis of Improved Crew Survivability in Light Vehicles Subjected to Mine Blast, Final report for contract no. DAAK70-92-C-0058 for the U.S. Army Belvoir RDEC, Ft. Belvoir, VA.

Neuberger, A., Peles, S., Rittel, D., 2007. Scaling the response of circular plates subjected to large and close-range spherical explosions. Part I: Air-blast loading. Int. J. Impact Eng. 34, 859–873.

Park, S., Uth, T., Fleck, N.A., Wadley, H.N.G., Deshpande, V.S., 2013. Sand column impact onto a Kolsky pressure bar. Int. J. Impact Eng. 62, 229–242.

Pickering, E.G., Chung Kim Yuen, S., Nurick, G.N., Haw, P., 2012. The response of quadrangular plates to buried charges. Int. J. Impact Eng. 49, 103–114.

Qiu, X., Deshpande, V.S., Fleck, N.A., 2005. Impulsive loading of clamped monolithic and sandwich beams over a central patch. J. Mech. Phys. Solids 53, 1015–1046.

Reichenbach, H., Behrens, K., Kuhl, A., 1991. Exploratory depth-of-burst experiments, Interim report, CONTRACT No. DNA 001-91-C-0039, Prepared for: DEFENSE NUCLEAR AGENCY, Washington, DC, USA.

Rimoli, J.J., Talamini, B., Wetzel, J.J., Dharmasena, K.P., Radovitzky, R., Wadley, H.N.G., 2011. Wet-sand impulse loading of metallic plates and corrugated core sandwich panels. Int. J. Impact Eng. 38, 837–848.

Rubino, V., Deshpande, V.S., Fleck, N.A., 2008. The dynamic response of end-clamped sandwich beams a Y-frame and corrugated cores, Int. J. Impact Eng. 35, 829-844.

Stout M. G., Follansbee P. S., 1986. Strain-rate sensitivity, strain hardening, and yield behaviour of 304L stainless steel. Trans. ASME: Journal of Engineering Materials Technology 108,344-353.

Taylor, L., Fourney, W., Leiste, U., 2010. Pressures on Targets From Buried Explosions, in: Proceedings of the IMPLAST 2010 Conference.

Tilbrook, M.T., Deshpande, V.S., Fleck, N.A., 2006. The impulsive response of sandwich beams: Analytical and numerical investigation of regimes of behaviour. J. Mech. Phys. Solids 54, 2242–2280.

Tremblay, J., 1998. impulse on blast deflectors from a landmine explosion, Technical Report DREV-TM-9814, Defence Research Establishment Valcartier, Quebec, Canada.

Uth, T., Deshpande, V.S., 2013. Unsteady penetration of a target by a liquid jet. Proc. Natl. Acad. Sci. U. S. A. 110, 20028–33.

Uth, T., Deshpande, V.S., 2014. The response of clamped sandwich beams subjected to loading via high-velocity sand slugs, Submitted to Int. J. Impact Eng.

Wadley, H., Dharmasena, K., Chen, Y., Dudt, P., Knight, D., Charette, R., Kiddy, K., 2008. Compressive response of multilayered pyramidal lattices during underwater shock loading. Int. J. Impact Eng. 35, 1102–1114.

Wadley, H.N.G., Børvik, T., Olovsson, L., Wetzel, J.J., Dharmasena, K.P., Hopperstad, O.S., Deshpande, V.S., Hutchinson, J.W., 2013. Deformation and fracture of impulsively loaded sandwich panels. J. Mech. Phys. Solids 61, 674–699.

Wei, Z., Deshpande, V.S., Evans, a. G., Dharmasena, K.P., Queheillalt, D.T., Wadley, H.N.G., Murty, Y.V., Elzey, R.K., Dudt, P., Chen, Y., Knight, D., Kiddy, K., 2008. The resistance of metallic plates to localized impulse. J. Mech. Phys. Solids 56, 2074–2091.

Westine, P., Morris, B., Cox, P., Polch, E., 1985. Development of computer program for floor plate response from land mine explosions, Contract Report No. 1345 for U.S. Army TACOM Research and Development Center.

Xue, Z., Hutchinson, J.W., 2004. A comparative study of impulse-resistant metal sandwich plates. Int. J. Impact Eng. 30, 1283–1305.

Zhang, J., Ashby, M., 1992. The out-of-plane properties of honeycombs. Int. J. Mech. Sci. 34.